Estimating Bounds on Coherent Acceleration and Velocity Pulses from Video-Recorded Rocking of Vehicles in Caraballeda during the M_w 7.5 Venezuela Earthquake

Garini E., Restrepo J.I., Gazetas G., Wu B. and Garcia-Gonzales R.M.

This manuscript is a non-peer-reviewed preprint submitted to EarthArXiv.

It has not yet undergone formal journal peer review.

Corresponding author: E. Garini

Affiliation: Technical University of Crete, Greece

ORCID: https://orcid.org/0000-0001-6972-5980

Journal status: Not yet submitted to a peer-reviewed journal.

Estimating bounds on coherent acceleration and velocity pulses from video-recorded rocking of vehicles in Caraballeda during the M_w 7.5 Venezuela earthquake

E. Garini, Ass. Professor, Technical University of Crete, Greece
J.I. Restrepo, Professor Emeritus, University of California, San Diego, USA
G. Gazetas, Professor Emeritus, National Technical University of Athens, Greece
Wu B, Postdoctoral Researcher, Scripps Institution of Oceanography, UC San Diego, USA
Garcia-Gonzales RM, PhD candidate, Scripps Institution of Oceanography, UC San Diego, USA

ABSTRACT

The lack of accelerograms in the heavily damaged coastal towns of La Guaira state north of Caracas to record the motions of the M_w7.5 earthquake motivate the present inverse analyses to estimate plausible ranges of coherent ground-velocity and acceleration pulse amplitudes at a particular coastal site. To this end, we utilize an exceptionally revealing video recorded by two CCTV stations during the event in the devastated town of Caraballeda, located a couple of hundred meters from the seismogenic fault, and about 35 km from the epicenter. The video shows a parked, unoccupied Daihatsu Terios SUV undergoing strong lateral rocking oscillations with substantial wheel uplift — evidence of very strong excitation. Analysing the car as a block supported on tensionless springs and dashpots of the wheel-suspension system and using as base excitation idealized wavelets (derived from two motions recorded under comparable seismologic and geotechnical conditions), we constrain plausible pulse amplitudes by comparing computed and observed peak rotation angles. A second heavier car, visually recognized as a Jeep Cherokee/Liberty KK SUV, is also seen in the video to undergo rocking oscillations, but with much smaller amplitude and little uplift. Reproducing its response to the same excitation provides an additional consistency check on the inferred pulse characteristics. The investigation demonstrates the potential of video-recorded nonlinear rocking responses to

provide *quantitative constraints* on (*rather than unique predictions* of) coherent near-fault seismic ground-motion pulses, at a location where no accelerogram is available.

INTRODUCTION: THE EARTHQUAKE AND ITS CONSEQUENCES

The second and larger of the earthquake doublet on 24 June 2026, of $M_w = 7.5$, originated on the San Sebastián Fault, a major right-lateral strike-slip (mostly offshore) fault, at the boundary between South American and Caribbean plates, as shown in Fig.1(a) (Audemard 2006, Colón et al 2015, Pousse Beltran et al 2016). The tectonics of the Caribbean–South American region is also sketched in Fig. 1(a), showing the different types of faulting between the five tectonic plates of the region. (See Dewey 1972, Schubert 1984, Perez et al. 2001, Mavroeidis & Papageorgiou 2008, Zimmerman et al 2023, Ahn & Lešková 2026, Beheshtian & Somerville 2026, Chaves et al 2026, Mangiagalli et al 2026).

The source of the M_w 7.5 event was the San Sebastián Fault [see Fig.1(b)]: originating at a small depth of about 10 km, the fault ruptured bilaterally for a total distance of about 200 km, terminating north-east of Caracas. The exact length of the rupture is being debated among seismologists, depending on whether the doublet is considered as a single seismic event or two separate ones. For details see Wong et al 2026, Riquelme et al 2026, USGS 2026, INGV 2026, Beheshtian et al 2026, Bustos et al 2026. Damage along the rupturing path seems to have been highest at the central Venezuelan coast 22 km – 35 km from the epicenter, as seen in Fig. 2, where the heavily damaged towns of Catia La Mar, La Guaira, and Caraballeda (all belonging in La Guaira state) are located (Gutierrez Soto et al 2026). In the town of Caraballeda numerous videos have shown the total collapse of several (modern-looking) multi-story buildings, among other collapses. A revealing map of a part near the coast of Caraballeda showing the locations of collapsed buildings is given in Fig.3, as reported in the damage map of the United Nations Satellite Centre (UNOSAT) after the satellite observations of Copernicus Emergency Management Service (CEMS). It is not surprising that these three towns suffered very heavy damage: in addition to lying on top of, or next to, the projection of the fault on the ground surface, they had many tall buildings, they

were founded on deep alluvial soil deposits, and they are located a sufficient distance (roughly 35 km) from the origin (the hypocenter). Thus, they would have experienced motions bearing forward-rupture directivity effects with significant long period velocity and acceleration pulses, as is generally known in seismology (Somerville et al 1997). Recall the Kahramanmaras M_W 7.8 earthquake in Turkey, 2023, the heaviest damage from which, and the strongest recorded ground motions, occurred in cities far from the origin (AFAD 2023, Abdelmeguid et al. 2023, Garini & Gazetas 2023). Deep soil deposits and non-horizontal topography may also have contributed substantially to the damage.

Indeed, the three towns are built on top of deep soil deposits originating from sediments transported from the mountains inland and deposited as coastal alluvial fans (Larsen et al. 2001). In broad terms, three distinct soil layers are encountered: the top relatively low-density sediments containing silt, sand, gravel and even boulders, followed by a denser alluvium, and finally by sedimentary rock, before reaching solid bedrock at great depths . The bedrock is not horizontal, but dips between 17 and 21 degrees towards the sea. Thus, at the seafront, the bedrock depth ranges from 180 m in Catia La Mar to 400 m in Caraballeda (Mangiagalli et al. 2026).

The 2026 earthquakes highlighted the region's inadequate preparedness, despite the historical record of strong earthquakes: an earthquake of magnitude M_w 7.3 had occurred in 2018 on the same fault towards the eastern end of the country, an M_w 6.7 earthquake in 1967 destroyed many tall and short buildings in Caracas (Seed et al. 1972), let alone the huge M 7.7 event in 1900 just 100± km east of Caracas, and the 2025 M_w 6.3 earthquake doublet WSW of this year's (2026) epicenters (Fig.4). Thus, unfortunately, there were no operating accelerograph stations in the heavily damaged towns of La Guaira State. Hence, no local accelerograms directly document the ground-motion characteristics in these heavily damaged towns. (Note that Bernal & Cardona 2026, derived artificial accelerograms for the three cities, using a seismological methodology, guided by

the distribution and intensity of damage along the rupture path, and computing in simple terms the effect of soil amplification.)

Fortunately, in the town of Caraballeda, located very close to the causative (seismogenic) fault, 35 km from the epicenter and 15 km north of Caracas, two closed-circuit television (CCTV) cameras mounted next to the door of a ground-floor sports center provided a video from the second, M_W7.5, earthquake. Fig. 5(a_1) shows the general plan view of the area, with the line of the Fault in Fig. 5(a_2) (approximately, as given by USGS 2026). In Fig. 5(a_3) we zoom-in on the location of the sports/bowling center, the CCTV cameras, and the plan location of the two SUV vehicles modelled here. The front view of the sports center and the cameras, along with a sketch of the plan area configuration are shown in Fig.5(a_4). A wealth of information could be extracted from this video to help uncover the fundamental characteristics of the ground motion at this particular site. Five immediate, conspicuous observations are made watching the video:

- Most of the people who ran out of the building, apparently escaping either immediately after the M_W7.2 earthquake's very weak shaking had stopped, or having just felt the P-wave arrivals, fell to the ground or clung to the fence.
- Seven or eight multi-storey buildings, including at least two 12-storey modern ones, collapsed spectacularly within the range of view of the cameras.
- A black waste bin touching the fence moved away by rolling and sliding for roughly 1.5 m, and another box-like block resting against the fence overturned.
- Several traffic delineator posts simply resting on the ground either overturned or moved by sliding away from their original position.
- The cars parked in the service road in front of the building vibrated primarily in lateral rocking mode. One SUV-type car, in particular, experienced violent oscillations with substantial uplifting of the wheels on one side.

The objective of the paper is to utilize the observed intense uplifting response of this car and obtain estimates of a fundamental component of the ground

motion, and specifically, the amplitude of the coherent long-period velocity pulse and the associated acceleration, that could have caused such a response. Recall the well-established destructive potential of such prevailing coherent pulses in near-source ground motions due to forward-rupture directivity effects (e.g. Baker 2007, Bertero et al. 1978, Sassani & Bertero 2002, Hall et al. 1995, Somerville & Graves 1993, Makris & Black 2004). Our analysis cannot distinguish the relative contributions to this motion of seismological factors, of soil-layer amplification, and of valley aggravation effects.

Indeed, the goal of this paper is *not* to investigate the factors that have contributed to the ground motion at the site, but only to estimate the resulting ground surface motion through its coherent "energetic" velocity and acceleration pulses, rather than to reconstruct detailed accelerograms. These estimates should be interpreted as a family of *ground motion constraints* consistent with the observed vehicle response, rather than as a unique reconstruction of the unrecorded earthquake accelerogram.

The response of a second, much heavier, SUV car which vibrated less intensely is also analysed to confirm the validity of, or modify, the results, using the same ground motion as excitation.

MODELLING OF THE STRONGLY UPLIFTED SUV-N_o1 VEHICLE

The severe rocking response of a parked, unoccupied, grey/silver car is clearly seen in the CCTV video to undergo the strongest rocking oscillations in the lateral direction, with substantial uplifting — evidence of very strong excitation. Having identified the car as a mid-size, second-generation Daihatsu Terios (from now on called either SUV-N_o1 or Daihatsu Terios), we estimate the peak angle of rotation of the vehicle, by examining the video frame-by-frame at the time-window of the strongest visible oscillation, using the "Kinovea" free software for the apparent rotation.

To account for camera motion, we used the software's motion-compensation feature, tracking fixed points on the fence as scene references to estimate the

CCTV movement during the earthquake. As a result, vehicle's visible rocking was quantified. The snapshots shown in Fig. 6 correspond to the largest uplifting moment of the car, initiating at 91.00 s and almost toppling at 91.50 s. But since the cameras were at a level higher than the car and recorded the vehicle at an angle from the side, while our target ("reality") is rocking oscillation about the vehicle's longitudinal base axis, the apparent angle underestimates the true rotation. To uncover the true perspective-corrected angle, we used the free software "Blender" with the addition of the "Polychase" tracking routine. Table 1 presents for specific times, the apparent and the perspective-corrected angles of rotation. From Table 1, accounting for uncertainty, we have: $35^o \lesssim |\theta_{max}| \lesssim 41^o$. The goal of our subsequent analyses is, by parametrically varying the excitation ground motion, to achieve a peak angle of rotation that matches the measured angle of $\mathbf{38^\circ \pm 3^o}$.

Table 1. Step-by-step recording of the apparent and the estimated actual rotation of Daihatsu Terios

CCTV Video instant time	*Apparent rotation measured in image*	*Perspective-corrected rotation ("reality")*	*Interpretation*
89.00 s	0°	0°	*reference orientation*
90.29 s	$+4.0^\circ$	$+12^\circ$	*opposite rocking extreme*
90.90 s	-8.9°	-28°	*clear unloading / uplift onset*
91.00 s	-11.5°	-36°	*near maximum observed roll*
91.50 s	-12.2°	$\boxed{-38^\circ}$	*maximum observed roll*

Having identified the car as a mid-size, second-generation Daihatsu Terios, we obtained from the manufacturer and related literature, its material and geometric

properties (Bixel et al. 2010, Dudziak et al. 2020, Han et al. 2022, Sadauckas et al. 2025, Soica & Gheorghe 2025, Zheng et al. 2015). Specifically:

- The mass, moment of inertia, track half-width, and height of the center of gravity are taken as:
  $\mathbf{m}$ = 1050 kg [1.05 t], $\mathbf{J_{CG}}$ = 350 kg.m^2 [0.35 t.m^2], $\mathbf{b}$ = 0.65 m, and $\mathbf{z_c}$ = 0.68 m. We note the height-to-base (aspect) ratio $\mathbf{z_c/b}$ ≈ 1.05 — a relatively squat body to undergo such substantial rotation.
- The support characteristics include: the axial (vertical) stiffness $\boldsymbol{k_z}$ = 22.5 kN/m of the wheel and suspension system of each support; the associated damping ratio $\boldsymbol{\xi_z}$ = 10% ; the lateral stiffness of each wheel-suspension system is $\boldsymbol{k_y}$ = 75 kN/m; the tyre-to-road coefficient of friction is $\boldsymbol{\mu}$ = 0.80; and the coefficient of restitution upon impact is $\boldsymbol{R}$ = 0.90.
- The stiffness of the two wheel-suspension systems of each side of the car is $\boldsymbol{K_z = 2\ k_z}$ = 45 kN/m, and the dashpot constant of each side corresponding to the above damping ratio $\boldsymbol{\xi_z}$ is given by $\boldsymbol{C_z = 2\ c_z = \xi\sqrt{K_z \cdot m/2}}$ ≈ 0.5 kN·s/m ($\boldsymbol{c_z}$ being the dashpot per wheel). The lateral stiffness of the two wheel-suspension systems of each side of the car is $\boldsymbol{K_y = 2\ k_y}$ = 150 kN/m. For 5% damping (appropriate for the lateral vibrations), $\boldsymbol{C_y = 2\ c_y = \xi\sqrt{K_y \cdot m/2}}$ ≈ 0.45 kN·s/m.

The above are representative values from the manufacturer and the related literature, which were subsequently varied parametrically to validate our conclusions. An extensive description of the lumped parameters of the model is omitted for brevity. However, a brief description of the most significant ones follows:

1. The value of vertical stiffness, $\boldsymbol{k_z}$, is estimated from the vertical frequency, $\boldsymbol{f_z}$, of the vehicle: Vehicle-suspension literature (Li et al. 2022, Zhu et al. 2014) typically places vehicle vertical frequency around 1.3–1.5 Hz for attaining acceptable comfort level for the passengers. A mean frequency of 1.39 Hz was

experimentally measured by Li et al. 2022. Therefore, for $f_z = \frac{1}{2\pi}\sqrt{\frac{2k_z}{m}} = 1.40$ Hz, we estimate the vertical stiffness k_z. The vertical stiffness includes the suspension coil stiffness, the vertical wheel compliance, and any other elastic compliances, in a lumped form.

2. At each side of the model, in addition to the vertical suspension spring, a lateral spring is attached with lateral stiffness k_y. Fathi et al. (2024) suggest a static lateral stiffness of 117 kN/m for their modelled passenger-car tyre, consistent with manufacturer reference values of 115–140 kN/m per tyre. Accordingly, an effective lateral stiffness of approximately 250 kN/m per side ($k_y = 125\ kN/m$, per tyre) is adopted as a reference for the heavier Jeep Cherokee/Liberty SUV (discussed later in the article). However, for the lighter Daihatsu Terios, a reduced lateral stiffness is considered appropriate, given its smaller tyres and lower wheel loads. Experimental findings indicate that lateral tyre stiffness depends on vertical wheel load and inflation pressure, with a nonlinear dependence on wheel load (op het Veld, 2008). In the absence of tyre-specific measurements, the effective lateral stiffness of the Terios is assumed to be approximately scaled with vehicle mass and the associated static wheel loads, while preserving a comparable characteristic lateral spring deformation at the Coulomb friction limit. Thus, a reduced value of $k_y = 75\ kN/m$ (per tyre), is selected as a representative modelling parameter.
3. Society of Automotive Engineers (SAE) test data on ordinary automotive tyres report dry-road locked-wheel friction coefficients around 0.7-0.9 (Lambourn & Wesley 2010) with peak friction values 1-1.2 depending on tire and pavement (Merritt et al. 2015). Thus, a tyre-to-road coefficient of friction μ = 0.80 is a reasonable basic value for our analyses.
4. A rigid-block rocking system under dynamic excitation exhibits a restitution coefficient, R, which depends on geometry (Housner 1963). However, this definition of restitution coefficient is for rigid-block and not for our study, where impact occurs through a pneumatic tyre-suspension system, not through a rigid block striking a rigid base. In our model, we take as nominal

value R = 0.90, adopting the findings of the experimental tyre-impact study of Sadauckas et al. (2025).

The car and a sketch of its lateral oscillation are pictured in Fig. 7, along with the 2D transverse cross-section modelled as a rigid body on two unilateral (tensionless) vertical wheel-suspension spring–dashpot pairs, two lateral springs and dashpots, all resting on the base with a Coulomb friction contact. The body rigidity is a realistic approximation given the large flexibility of the suspension system in vertical and rocking mode, and the limited frictional capacity of the wheel-base contact. The Center of Gravity (CG) can move laterally and vertically, while undergoing rotation. Its three generalized coordinates are: u_y lateral translation, u_z vertical translation, and θ total rotation about the car's longitudinal x axis. The vertical translation is explicitly taken into account for assessing the (usually second-order) P – Δ effects, important here to account for the large angles of rotation and uplifting.

The *full-contact ("elastic")* formulation follows the general rigid block on compliant-foundation dynamics (see for example Gazetas 1983), where the role of rotational soil stiffness is played by the vertical springs:

$K_\theta = 2\,K_z b^2 = 4 k_z b^2$ = 38 kN·m /rad. To approximate the rocking fundamental period T_θ of the car for full-contact vibrations the appropriate mass moment of inertia is with respect to the base center rather than the center of gravity: $J_o = J_{CG} + m z_c^2 \approx 0.84$ t·m^2. Thus,

$$T_\theta \approx 2\pi \sqrt{\frac{J_o}{K_\theta}} \approx 0.91 \text{ s} \quad (1)$$

T_θ increases upon uplifting, tending theoretically to an infinitely large value at the verge of *static* instability, i.e. when the angle of rotation θ reaches $\theta_c = \arctan(b/z_c) \approx 44^o$, and the motion is about to stop. Of course, under *dynamic* seismic conditions the angle of instability is larger (Adamidis et al. 2014, Apostolou et al. 2007, Apostolou 2011, Farazmand et al. 2025, Figini & Paolucci 2017), and this must be kept in mind when reviewing some subsequent results. The substantial

increase of the period of the oscillating car is evident in the video at the moment of the largest uplift rotation.

The governing equations of motion are:

$$\begin{aligned} m\ddot{u}_y &= T_L + T_R - m\ddot{u}_g \\ m\ddot{u}_z &= N_L + N_R - mg \\ I_G\ddot{\theta} &= d_1 N_L - d_2 T_L + d_3 N_R - d_4 T_R \end{aligned} \tag{2}$$

where: $\ddot{u}_g$ is the earthquake ground acceleration (imposed as base excitation); N_L and N_R are the vertical reaction forces on the LEFT and RIGHT sides of the vehicle (sum of the two reactions of the front and back wheels); T_L and T_R are the horizontal traction force at the LEFT and RIGHT sides of the vehicle; and d_1, d_2, d_3, d_4 are the lever-arms of reaction and traction forces from the CG:

$$\begin{aligned} d_1 &= -b \cdot \cos\theta + z_C \cdot \sin\theta \\ d_2 &= -b \cdot \sin\theta - z_C \cdot \cos\theta \\ d_3 &= +b \cdot \cos\theta + z_C \cdot \sin\theta \\ d_4 &= +b \cdot \sin\theta - z_C \cdot \cos\theta \end{aligned} \tag{3}$$

Notice that for vanishingly small θ ($\sin\theta \approx 0$, $\cos\theta \approx 1$) the lever arms reduce to the more familiar from low-amplitude foundation dynamics : $d_1 \approx -b$; $d_2 \approx -z_C$; $d_3 \approx b$; $d_4 \approx -z_C$.

Finally, the relation between forces and response displacements and velocities (with compression being positive) are:

$$(N_L, N_R) = K_z\, u_z + C_z\, \dot{u}_z \geq 0 \qquad \text{uplifting when } (N_L, N_R) = 0 \tag{4a}$$

$$\begin{aligned} (|T_L|, |T_R|) &= K_y |u_y| + C_y |\dot{u}_y| \\ &\leq \mu(|N_L|, |N_R|) \end{aligned} \qquad \begin{aligned} &\text{sliding when } (|T_L|, |T_R|) = \\ &\mu\,(|N_L|, |N_R|) \end{aligned} \tag{4b}$$

The total angle of rotation is then divided into an "elastic" (i.e., full-contact) and an uplifting part:

$$\theta(t) = \theta_{el}(t) + \theta_{up}(t) \tag{5}$$

Keep in mind that the term “elastic” is only used for brevity; in reality it is “viscoelastic” — hence the quotation marks. In the sequel, the peak values of angles of rotation are simply denoted as θ, θ_{el}, θ_{up} .

Then from the many available worldwide earthquake near-fault motions recorded on strike-slip faults, we selected two records with recognized forward-rupture directivity effects, choosing components close to the fault-normal direction, as is appropriate for Daihatsu Terios (recall Fig. $5a_3$). Indeed, the car is not parallel to the fault, but forms an angle of about 20°. Hence, what we are searching for, is not only the likely Fault Normal (FN) component, but also one 20° from the (expectedly more intense) FN. Another video (not shown here, but available in YouTube) shows a truly dramatic water sloshing across the short side of a small private swimming pool, whose long side is almost parallel to the fault; the huge and violent water splashing laterally out of the long side of the pool is a strong confirmation of the huge intensity of the FN motion. (See Somerville 2000.)

The two records selected are Fukiai EW (Kobe 1995) and Lixouri EW (Cephalonia 2014), both exhibiting clear and strong forward-rupture directivity effects. Specifically, the Fukiai accelerogram, at a site about 30 km from the origin, 1 km from the seismogenic fault, has an EW component of similar inclination (of about 20° – 25°) to the Kobe M_{JMA} 7.2 fault direction — hence it is suitable to use. The Lixouri EW component was a true FN motion, recorded near the end of the fault rupture, about 15 km from the epicenter and less than 1 km from the fault projection (Sokos et al. 2015), next to the strike-slip fault, but from a smaller magnitude M_w 6.1 event (Garini et al. 2017). Nevertheless, the smaller than M_w7.5 magnitude is still acceptable as a reference motion, since for short distances from the fault, substantial distances from the origin of the event, and dominant periods between 1 and 2 seconds, the effect of the exact magnitude is insignificant (Somerville et al. 1997). Both of these records have also been affected to an appreciable degree by soil amplification-type filtering, as undoubtedly were the motions in Caraballeda (Bernal & Cardona 2026).

To each velocity time-history, V(t), of these motions we fitted *optimally* several idealized types of wavelets (Garini et al. 2014, Vassiliou & Makris 2011)

which included a few from M&P (Mavroeidis & Papageorgiou 2003) and from Gabor (Gabor 1946). The acceleration histories, A(t), were calculated analytically from the fitted velocity histories — hence their fitting is not as close as that of the velocity. The pulse duration was about 5 seconds, which is a little smaller than the 7 seconds of strong ground motion noticed and mentioned in the CCTV video, but it leads to total strong duration of the motion of the cars' response of more than 7 seconds. (We further explore this issue in the sequel.) The bilateral rupture, the forward-rupture directivity, and the reported high rupture velocity, V_R ≈ 3.8 km/s, of a part of the fault (Bernal & Cardona 2026, Wong et al. 2026) may explain such a short duration.

A very good fit for these particular motions was found to be with asymmetric Gabor as seen in the comparison of Fig. 8 for the Fukiai and Lixouri motions, and thus it was the one type of wavelet mostly utilized here. But the M&P wavelets, possibly offering a preferred fit to another motion not considered here, are also used for better constraining the resulting motions. Seismologically-based simulations by Bernal & Cardona (2026) confirm, in their own words, *"that the rupture generated pronounced velocity pulses characteristic of earthquakes exhibiting strong forward directivity, concentrating a substantial portion of the released seismic energy within relatively short time intervals"*— in accord with our assumptions regarding the selection of ground motions. It should be noted that the direction of lateral response of the car is not exactly normal to the fault, forming an angle of about 20°; hence our selection of the EW component of Fukiai, which also formed a similar angle with the Kobe fault normal. Although our analyses are for *two types of wavelets*, an asymmetric Gabor and an M&P, other wavelet choices have been found (in few analyses) to produce *predictably small* differences in the final inferred intensities, in agreement with Bustos et al. (2026), Jampole et al. (2018), and Makris & Black (2004).

Table 2. Computed angles of rotation of the Daihatsu Terios car caused by (parametrically varying) Fukiai-based Gabor wavelet

A_{Gabor} (g)	V_{Gabor} (m/s)	θ (degrees)	θ_{up} (degrees)
0.40	1.03	19	11
0.43	1.11	24	17
0.45	1.16	29	22
0.48	***1.24***	***38***	***30***
0.50	1.30	44	36
0.51	1.32	Toppling	

ANALYSIS AND RESULTS: FUKIAI-BASED GABOR EXCITATION OF SUV-N_o1 VEHICLE

The dynamic equilibrium equations are solved by ***direct numerical time integration.*** The second-order equations are transformed into a first-order system of ordinary differential equations, supplemented by internal state variables describing frictional sliding of the wheels. The resulting initial-value problem is solved using the "DOP853" explicit Runge–Kutta method of order 8, as implemented in the "Python SciPy" library through the "solve_ivp" routine (Hairer et al. 1993, Virtanen et al. 2020). Each Gabor wavelet, which was imposed as excitation, was scaled to 6 different values of peak acceleration, A_{Gabor}, and peak velocity, V_{Gabor}, in search of the values that lead to an angle of rotation of about 35° – 41°. Table 2 shows the studied pairs and the resulting angles of rotation.

The successful asymmetric Gabor wavelet of $\mathbf{T_p \approx 1.5\ s}$ that gives a resulting maximum angle of rotation of the Daihatsu Terios consistent with that observed in the video, ≈ 38°, is the motion with $\mathbf{A_{Gabor} \approx 0.48\ g}$ and $\mathbf{V_{Gabor} \approx 1.24\ m/s}$. Detailed results of the analysis are shown for this successful motion in Figures 9 – 12. Specifically:

- Figure 9 summarizes the parametric search for the optimum amplitudes of acceleration (and the associated velocity). The figure plots rotation

time histories with reference to A_{Gabor}. It is evident that the motion having $A_{Gabor} \approx 0.48$ g and $V_{Gabor} \approx 1.24$ m/s leads indeed to the result closest to the observation as seen in Table 2.

- Fig. 10 compares the acceleration A(t), velocity V(t), and displacement D(t) of the base excitation with those obtained for the center of mass of the vehicle. Notice that whereas their accelerations and velocities are not very different (except for the longer total duration of the response), the horizontal displacement of the car center (in the negative y direction) exceeds that of the base by a factor of about 1.60. And, more significantly, the duration of this exceedance is almost 2 seconds (corresponding to an effective response period of approximately 2.5 s) — evidence of the increased effective period during large uplifting angle. As already mentioned, this is consistent with the observed response of the car.
- Fig. 11 compares the time histories of the elastic and the uplift angles of rotation, confirming the large uplift with long duration interval, as noted above.
- Fig. 12 plots the time histories of the normal reactions, N, acting from the ground against the wheels of each of the two sides (left and right), and contrasts them with the time history of the uplift angle. Uplifting occurs when the normal reaction N = 0. It can be recognized in this figure at what time exactly uplifting takes place, and on which side. Again, notice the 2.5 s (±) of the uplift duration of the right wheel.

The success of the model and the analysis stem not only from matching the observed peak angle of rotation, but also from the proper qualitative anticipation of the asymmetric uplift and, especially, from explaining the large duration of the major uplift.

Our parametric study included variation in the axial stiffness from 40 kN/m to 50 kN/m, as indicated in the literature. Differences in the outcome exist but are too small to warrant illustration here (see a related comparison later on). Also not shown here is the time history of the *slippage* of the wheels, as its peak magnitude was only 2–5 cm in the various parametric analyses.

INCREASING THE DOMINANT PERIOD OF FUKIAI-BASED GABOR EXCITATION OF SUV-N$_o$1

However, there is a possibility that the ground motion had a larger dominant period than the $T_p \approx 1.5$ s of the Fukiai-based Gabor. The substantial distance (≈ 35 km) of the site from the starting point (the hypocenter) and the large depth of the soil deposit would justify a slightly longer velocity pulse. We chose the increase of time by a factor 7/5 = 1.4, to have an overall time of the strong motion equal to 7 s, as the video shows, rather than the 5 s of the current Gabor. Thus, in this case, the dominant period is 1.5 × 1.4 = 2.1 seconds. An impulsive motion with this large velocity period might be considered as a very unfavourable estimate of the likely motion. The velocity time history V(t) of the stretched Gabor motion of A_{Gabor} = 0.48 g and velocity V_{Gabor} = 1.73 m/s is shown in Fig. 13 in comparison with that of the original motion (which was of the same A_{Gabor} = 0.48 g, but of smaller $V_{Gabor} \approx 1.24$ m/s).

The computed response of the light Daihatsu Terios to this motion shows *overturning collapse*, as seen in the parametric search of Fig. 14 — rather unsurprisingly, since in this case the peak velocity, 1.73 m/s, is much greater (by a factor of 1.4) than the 1.24 m/s of the initial unstretched Gabor velocity. Recall that large peak velocity (and velocity increment) is the most detrimental measure of intensity for inelastic systems (Bertero et al. 1978, Garini & Gazetas 2013, Sassani & Bertero 2002, Hall et al. 1995).

By parametrically downscaling the stretched motion to A_{Gabor} = 0.30 g, 0.40 g, 0.42 g, 0.45 g, 0.46 g (and correspondingly the velocity V_{Gabor}) we obtain the response angles of rotation that are compared in Fig. 14 . Evidently, the A_{Gabor}= 0.45 g motion is the one whose response of 40^o matches closely enough the peak observed angle of about 38^o. The corresponding peak velocity, however, is V_{Gabor} ≈ 1.60 m/s. Fig. 15 presents the total θ(t) and uplift $\theta_{up}(t)$ rotation, and Fig. 16 contrasts $\theta_{up}(t)$ with the axial reactions N(t) from the ground against the two wheels. The similarity of the results to those in Figures 10–12 for the original Gabor wavelet of 0.48 g and 1.24 m/s is evident.

In conclusion, an asymmetric Gabor motion fitted to the stretched Fukiai motion, with dominant period $\mathbf{T_P \approx 2.1\ s}$, peak velocity $\mathbf{V_{Gabor} \approx 1.60\ m/s}$ and peak acceleration $\mathbf{A_{Gabor} \approx 0.45\ g}$, could explain the rotational response of the Daihatsu Terios car during the Venezuelan M_W7.5 Earthquake.

To investigate a still longer dominant period, we further stretched the Fukiai motion leading to a fitted Gabor wavelet with dominant spectral $S_V(T)$ period of $\mathbf{T_P \approx 2.5\ s.}$ This new wavelet led to peak angle of rotation $\theta \approx 38°$ when it was downscaled to achieve values of $\mathbf{V_{Gabor} \approx 1.85\ m/s}$ and peak acceleration $\mathbf{A_{Gabor} \approx 0.42\ g}$. For the sake of brevity, the results of this study are not presented here.

RESULTS FOR THE LIXOURI-BASED GABOR EXCITATION OF SUV-N_O1 VEHICLE

The Lixouri (2014) strike-slip, fault-normal, motion bears a strong forward directivity effect (Garini et al. 2017) and has PGA = 0.62 g and PGV = 1.18 m/s. As seen in Fig. 17 the motion can be fitted readily by a Gabor wavelet with velocity of amplitude V_{Gabor} = 1 m/s and acceleration A_{Gabor}= 0.47 g. These are very close to the optimal values obtained with Fukiai-based Gabor, as shown below. Moreover, the dominant period of V(t) of the two fitted motions is nearly the same (about $T_p \approx 1.5$ s) as seen in the velocity response spectrum, $S_V(T)$, given in this Fig. 17; but the duration is somewhat shorter than the 7 seconds of strong motion duration.

The response of the Daihatsu Terios car is explored parametrically in Fig. 18, by down- and up-scaling the original fitted Gabor, varying its amplitudes from A_{Gabor}= 0.35 g – 1.0 g. It is readily noted that the best outcome, $\theta \approx 38^o$ of the right side of the car, is achieved for $\mathbf{A_{Gabor}= 0.50\ g}$ and, correspondingly, $\mathbf{V_{Gabor} = 1.20\ m/s}$ — indeed very similar to the initial values before scaling. Notice that some of the higher accelerations give either unattainable or erroneously "early" rotations of the left side of the car, contrary to the observation.

Therefore, the Lixouri fitted Gabor (0.50 g, 1.20 m/s) that is compatible with the observed rotation has a little higher acceleration and a little smaller velocity than those of the Fukiai-based motion (0.48 g, 1.24 m/s). These are small differences indeed.

RESULTS FOR THE LIXOURI- AND FUKIAI-BASED MAVROEIDIS-PAPAGEORGIOU (M&P) WAVELETS

To explore the sensitivity, and improve the constraint, of our results, the M&P wavelets fitted to the two seismic motions, shown in Fig. 8, are used in our reverse analysis of the Daihatsu Terios car. Fig. 19 shows the velocity and acceleration response spectra of these wavelets. The parametric results are plotted in Figures 20 and 21 for Fukiai- and Lixouri-based M&P wavelets, respectively, while Table 3 summarizes the main results. Each of the two figures compares the angles $\boldsymbol{\theta}(t)$ and $\boldsymbol{\theta_{up}}(t)$ for ten different peak values of excitation, designated in terms of $A_{M\&P}$.

Table 3. Computed peak angles of rotation of Daihatsu Terios caused by (parametrically varying) Fukiai- and Lixouri-based M&P wavelets

Original Motion	$A_{M\&P}$ (g)	$V_{M\&P}$ (m/s)	Peak A_{CG} (g)	θ (°)	θ_{el} (°)	θ_{up} (°)
Fukiai (fitted with M&P)	0.50	1.30	0.69	28	15	21
	0.51	1.32	0.66	30	14	22
	0.52	1.34	0.62	32	13	25
	0.53	1.37	0.62	35	12	28
	0.54	***1.39***	***0.63***	***38***	***12***	***31***
	0.55	1.42	0.71	42	15	34
	0.60	1.55	Toppling			
	0.65	1.68	Toppling			
	0.70	1.81	Toppling			
	0.80	2.07	Toppling			
Lixouri (fitted with M&P)	0.48	1.03	0.73	24	16	16
	0.50	1.07	0.72	28	16	19
	0.52	1.12	0.68	32	15	24
	0.54	1.16	0.62	36	13	28
	0.55	***1.18***	***0.63***	***38***	***12***	***31***
	0.57	1.22	0.70	45	15	37
	0.58	1.24	Toppling			
	0.59	1.26	Toppling			
	0.60	1.29	Toppling			

It is evident that the values leading to θ = 38^{o} are, for Fukiai and Lixouri based wavelets, respectively:

$$\mathbf{A_{M\&P} = 0.54\ g}\ \text{ and }\ \mathbf{V_{M\&P} = 1.39\ m/s}$$

$$\mathbf{A_{M\&P} = 0.55\ g}\ \text{ and }\ \mathbf{V_{M\&P} = 1.18\ m/s}$$

Therefore, the two types, Gabor and M&P, of the "successful" wavelets have similar peak velocities, but the M&P wavelets require a little larger peak acceleration to lead to the uplift of the light car. It is not obvious where this difference comes from. Notice only in Fig. 8, that the M&P motions are "truncated" by excluding one more trailing cycle: they have 3 or 4 peaks instead of the 4 or 5 peaks, respectively, of the asymmetric Gabor. It is also worth noticing that $\boldsymbol{\theta}$(t) of the M&P excitations in Figs 20 and 21 are much smoother than those of Gabor (Figs 11, 15, 18). We do not claim that the above two observations are the reasons for the differences, which in any case are very small.

ANALYSIS OF ROCKING OF THE HEAVIER SUV-No2 VEHICLE

To provide an additional check on the inferred idealized wavelet motions that explained the behaviour of the Daihatsu Terios car, we investigate the response of a relatively tall but much heavier car, seen in Fig.22. We identified it visually as a *Jeep Cherokee/Liberty KK* (called either SUV-N$_o$2 or Jeep Cherokee/Liberty). Its material and support parameters (from the manufacturer and the literature: Chrysler 2007, Czarnecki 2008, Li et al. 2022) are given in Table 4:

Table 4. Inertial and stiffness properties of Jeep Cherokee/Liberty KK

m = 1900 kg	$\mathbf{J_{CG}}$ = 850 $\mathrm{kg \cdot m^2}$
b = 0.82 m	$\mathbf{z_c}$ = 0.85 m
$\mathbf{K_z}$ = 90 ÷ 100 kN/m	$\mathbf{K_y}$ = 250 ÷ 300 kN/m
$\mathbf{C_z}$ = 1.35÷ 1.50 kN·s/m	$\mathbf{C_y}$ = 3.08 ÷ 3.5 kN·s/m

The *full-contact ("elastic")* formulation follows the general rigid block on compliant-foundation dynamics (see Gazetas 1983), where the role of rotational soil stiffness, K_θ, is played through the vertical springs:

$$K_\theta = 2\,K_z b^2 = 4\bar{k}_z\, b^2 = 121 \text{ kN}\cdot\text{m/rad}.$$

The proper mass moment of inertia is the one with respect to the base center rather than the center of gravity: $J_o = J_{CG} + m\,z_c^2 \approx 2.22 \text{ t}\cdot\text{m}^2$. Thus,

$$T_\theta \approx 2\pi \sqrt{\frac{J_o}{K_\theta}} \approx 0.85 \text{ s} \qquad (6)$$

a value very slightly smaller than that of the Daihatsu Terios.

The above are average values between those given by the manufacturer. Note that the height-to-base (aspect) ratio $\mathbf{z_c/b} \approx 1.04$, is practically the same as that of the Daihatsu Terios car. Thus, the main differences between the two cars with respect to rocking are the larger mass (by a factor of 1.8), larger mass moment of inertia (by 2.5), and larger stiffness (by 3.2) of the Jeep Cherokee/Liberty. Hence, the expectation of smaller rotation (e.g., Housner 1963, Makris & Roussos 2000).

Table 5. Step-by-step estimation of the apparent and the likely-actual Jeep Cherokee/ Liberty rotation

CCTV Video instant time (s)	*Apparent rotation measured in image (degrees)*	*Perspective-corrected rotation, the "reality" (degrees)*	*Interpretation*
87.00 s	0°	0°	*reference orientation*
90.29 s	$+3.14^\circ$	$+9.82^\circ$	*opposite rocking extreme*
90.50 s	-2.18°	-6.81°	*clear unloading / uplift onset*
90.71 s	-4.89°	-15.29°	*near maximum observed roll*
90.75 s	-5.06°	$\boxed{-15.82^\circ}$	*maximum observed roll*

We estimated the maximum angle of rotation, θ, by examining the video frame-by-frame in the time window of the strongest visible oscillation, using the aforementioned methods explained for the Daihatsu Terios car. The results are shown in Table 5.

Accounting for greater uncertainty due to the location of the car in front of the camera, we conclude that: $\mathbf{13^o \lesssim |\theta_{max}| \lesssim 20^o}$**,** with a most probable value of **16° .**

For the car's 2D model (Fig. 22), the governing Eqns (2) are solved with the new parameters of the Jeep Cherokee/Liberty, using as base excitation the successful (for the Daihatsu Terios) **Fukiai-based** asymmetric Gabor having A_{Gabor} = 0.48 g, V_{Gabor} = 1.24 m/s. The response to this motion of the heavier car, also shown in Fig. 22, shows that the peak angles

$$\boldsymbol{\theta_{up} \approx 13^{\,o}} \text{ and } \boldsymbol{\theta \approx 22^{o}} \qquad (6)$$

come close to matching the highest estimate of observed rotation, $\theta \approx 20^o$, but it is larger than the most probable angle, $\boldsymbol{\theta \approx 16^o}$.

However, the **Lixouri-based** Gabor wavelet (A_{Gabor} = 0.50 g, V_{Gabor} = 1.20 m/s) leads to an angle of the heavy car a little smaller: ≈ **19.6^o —** closer to "reality". Furthermore, see in Fig. 23 the results of parametrically investigating the effect of the vertical stiffness (K_z) of the heavy Jeep Cherokee/Liberty car on the total and uplifting angles. The excitations are the **Lixouri-based** Gabor with A_{Gabor} =0. 50 g, V_{Gabor} = 1.2 m/s (left) and the Fukiai-based Gabor with A_{Gabor} =0. 48 g, V_{Gabor} = 1.24 m/s (right), i.e. the scaled motions that were found to lead to response angles of the light Daihatsu Terios car similar to the measured $\theta \approx 38^o$. For assumed K_z = 90 kN/m and 100 kN/m, the two wavelets could lead to a peak angle of rotation closer to the observed range, $13^o - 20^o$.

For further insight into the uncertainties of the problem, Table 6 summarizes the results of a more detailed parametric study. The conclusion from the Table is that, within the unavoidable uncertainty on the wavelet peak amplitudes of acceleration and velocity, in addition to that of the vertical stiffness, the motions that explain the large rotation of the light Terios car can also explain the smaller

rotation of the heavy Jeep Cherokee/Liberty, after perhaps *a very-slight decrease* in its A and V amplitudes. This provides an additional, though less precise, consistency check on the inferred pulse amplitudes.

Table 6. Parametric results for peak angles of rotation of the heavy Jeep Cherokee/Liberty SUV, varying the vertical stiffness and the peak acceleration and velocity of the Gabor wavelets.

Original Motion	K_z (kN/m)	A_{Gabor} (g)	V_{Gabor} (m/s)	Peak $A_{c.g.}$ (g)	θ (°)	θ_{el} (°)	θ_{up} (°)
Lixouri (fitted with Gabor)	**90**	0.40	1.03	0.82	12	9.6	7
		0.50	***1.20***	***0.87***	***20***	***12***	***16***
		0.55	1.42	0.97	27	11	21
		0.60	1.55	1.12	28	11	22
	100	0.40	1.03	0.74	10	8	5
		0.50	***1.20***	***0.93***	***17***	***11***	***12***
		0.55	1.42	1.07	21	11	15
		0.60	1.55	1.19	24	12	16
		0.65	1.67	1.18	27	12	19
Fukiai (fitted with Gabor)	**90**	0.40	0.89	0.95	14	11	10
		0.48	***1.07***	***0.97***	***20***	***14***	***16***
		0.50	1.11	0.96	22	14	25
		0.55	1.22	0.82	29	14	23
		0.60	1.34	0.87	34	14	29
	100	0.40	0.89	0.97	11	10	0
		0.48	***1.07***	***1.05***	***19***	***13***	***17***
		0.50	1.11	1.05	20	13	20
		0.55	1.22	0.92	26	13	21
		0.60	1.34	0.97	30	13	26

WHAT ABOUT THE VERTICAL COMPONENT OF GROUND MOTION?

All analyses so far assumed the excitation to be solely a horizontal motion. Therefore, the previous conclusions are valid only under this assumption. But an earthquake ground motion always contains a vertical component. We have to investigate the effect of this simultaneously occurring component.

Shallow strike-slip faulting has produced in many cases very weak vertical ground motions. As an example, we attach in Table 7 the list of peak accelerations and peak velocities of the strong motions of the Kobe 1995 earthquake, in terms of the direction of each component. Notice that the *vertical acceleration* peaks are only a fraction (on average 40 %) of the Fault-Normal (FN) peaks, while the *vertical velocity* peaks are an even smaller fraction (only 20 %) of those of the FN.

Table 7. PGA (m/s^2) and PGV (cm/s) of each component of strong records from Kobe 1995. Adapted from Miyazaki et al. (2023).

Station	Record Component	PGA (m/s^2)	PGV (cm/s)
Kobe JMA	NS	8.18	91
	EW	6.17	76
	FN	**8.46**	**105**
	UD	3.32	40
FUKIAI	NS	6.86	57
	EW	8.02	123
	FN	**8.32**	**130**
	UD	—	—
TAKATORI	NS	6.42	133
	EW	6.66	127
	FN	**7.59**	**165**
	UD	2.89	16
Kobe D8T (Dai 8 Tottei)	NS	6.83	182
	EW	3.94	61
	FN	**7.28**	**189**
	UD	3.41	35

Nevertheless, we use the original Lixouri vertical acceleration time history, whose $PGA_V \approx 0.5$ g is equal to 80 % of the horizontal $PGA_H \approx 0.63$ g, in order to get an illustrative upper-range estimate of the effect of the *vertical motion*. The records of the two components are shown in Fig. 24.

First, both components, unchanged (that is, as recorded, without any wavelet fitting), are used as simultaneous excitation to capture properly the much higher frequencies contained in the vertical component. Fig. 25 compares the response to excitation ***without*** and ***with*** the vertical excitation. The resulting peak rotation angles in the two cases are almost equal (36^o versus 37^o), both slightly

inferior to the actual angle of rotation, despite the 0.63 g peak horizontal acceleration and 1 m/s peak horizontal velocity. (Obviously, the latter, being the most critical of the two parameters, is quite small.)

As a parametric investigation, Gabor wavelets are now optimally fitted to the vertical component's V(t) and, along with the Gabor wavelet of the horizontal component, excite the car. Moreover, to be certain of the polarity (up or down) of the vertical motion, we perform two analyses with the vertical component applied either with (+) or with (–) sign. The results are summarized in Fig. 26, and it is really interesting to see that the effect of the vertical component is small for the motions examined for these pulsive motions, leading to a change of only approximately ± 2–3 % in peak total rotation relative to horizontal excitation alone (Fig. 26).

There is no evidence of much more substantial vertical acceleration in Caraballeda than in Lixouri. In the video, the lid of the black waste-bin did not move upward at all (it was personally checked that it was indeed free to do so), and the white-black bin toppled without any apparent vertical jumping. We can thus, tentatively at least, conclude that the results of the previous sections, where only horizontal excitations were imposed, are approximately valid. Note that similar conclusions regarding the negligible effects of the vertical component of motion for both rocking and sliding systems can be seen in Gazetas et al (2012), Tsopelas et al. (1996), Bustos et al. (2026), among others.

SUMMARY AND CONCLUSIONS

The recorded rocking response of two parked vehicles in Caraballeda provided an unusual opportunity to constrain the characteristics of strong earthquake ground motion at a site of no instrumental recordings. A nonlinear dynamic model of a block undergoing swaying–rocking oscillations, incorporating suspension flexibility, unilateral contact, uplifting, and frictional sliding, was used to identify idealized coherent ground-motion pulses capable of reproducing the observed large-amplitude rocking of a Daihatsu Terios SUV.

Within the investigated families of asymmetric Gabor and M&P wavelets, and the adopted vehicle properties, the compatible ground motions have dominant velocity-pulse periods, $\mathbf{T_p}$, in the range of **1.5 s – 2.5 s**, pulse velocity amplitudes, **V**, in the range of **1.2 m/s –1.85 m/s**, and corresponding pulse acceleration amplitudes, **A**, of **0.42 g – 0.55 g**. The response of a second, heavier vehicle provides an additional, although less precise, constraint on the estimated excitation. These estimates should be interpreted as a family of ground motions compatible with the observed response of the two vehicles, rather than as a unique reconstruction of the unrecorded earthquake accelerogram.

Moreover, the actual peak ground acceleration (PGA) remains less constrained because the high-frequency components and random fluctuations of ground shaking have been excluded in our reverse procedure. Consequently, the actual PGA, and to a lesser extent PGV, may exceed the fitted pulse amplitudes A_{Gabor}, $A_{M\&P}$ and V_{Gabor} and $V_{M\&P}$. The accelerograms of Fukiai and Lixouri in Figure 8, compared with the fitted wavelets, provide indicative, record-specific ratios between peak ground-motion values and fitted pulse amplitudes:

- For Fukiai : $PGA/A_{Gabor} \approx 0.80/0.50 = 1.60$ and $PGV/V_{Gabor} \approx 1.35 / 1.2 \approx 1.12$
- For Lixouri : $PGA/A_{Gabor} \approx 0.62 /0.47 \approx 1.35$ and $PGV/V_{Gabor} \approx 1.2 / 1.1 \approx 1.10$

Even though the sample is very small for a general statistical conclusion, the following site- and orientation-specific ranges should be regarded as tentative extrapolations rather than direct results of the inverse analysis:

$$\mathbf{PGA \approx 0.60\ g – 0.80\ g} \text{ and } \mathbf{PGV \approx 1.25\ m/s – 1.90\ m/s} \quad (7)$$

If the limited directional information in Table 7 is used only as an approximate guide for the discrepancy between the FN and a component at 25° to the Fault, a multiplying factor of 1.05 could be applied to the above values to illustrate possible fault-normal (FN) peak values:

$$\mathbf{PGA_{(FN)} \approx 0.65\ g – 0.85\ g} \text{ and } \mathbf{PGV_{(FN)} \approx 1.30\ m/s – 1.95\ m/s} \quad (8)$$

In view of the huge number of total collapses of modern multi-story buildings, especially along and near the fault line in Caraballeda, the higher end of the

illustrative range in Eq. (8) merits consideration, although building damage alone cannot establish the local PGA or PGV. If confirmed, these PGV estimates would rank among exceptionally large values (for comparison, larger velocities have been reported at: *Rinaldi,* in Northridge 1994; *TSU068,* in Chi-Chi 1999; and *Antakya 3123,* in Kahramanmaraş 2023).

Although the inverse analysis involves unavoidable modelling and observational uncertainties, the investigation demonstrates the potential of video-recorded nonlinear rocking responses to provide quantitative constraints on coherent seismic near-fault ground-motion pulses at locations where no instrumental measurements are available. Reverse analyses by other investigators: (a) have found higher velocity amplitudes, of about **2 m/s,** using sliding objects as observation specimens for analysis (Bustos et al. 2026, Restrepo et al. 2026), and (b) have found smaller velocity amplitudes, **≤ 1 m/s** using seismological modelling (Bernal & Cardona 2026, Wong et al. 2026).

ACKNOWLEDGEMENT

Gratitude is owed to Mr. José Elías Naassaneh, owner of the La Guaira Bowling Center, for disseminating the closed-circuit television footage which formed the basis of our study.

REFERENCES

(a) Free Software

Kinovea Software: https://www.kinovea.org/

Blender : https://www.blender.org/

Polychase (Version 0.0.14) for Blender: https://extensions.blender.org/add-ons/polychase/

(b) Published Papers and Reports

Abdelmeguid M, Zhao C, Yalcinkaya E, Gazetas G, Elbanna A, Rosakis AJ (2023) "Dynamics of episodic supershear in the 2023 M7.8 Kahramanmaraş/Pazarcik earthquake, revealed by near-field records and computational modeling", *Communications Earth and Environment*, Article **4**:456

Adamidis O, Gazetas G, Anastasopoulos I, Argyrou C (2014). “Equivalent-linear stiffness and damping in rocking of circular and strip foundations”. *Bulletin of Earthquake Engineering* **12**(3): 1177–1200.

AFAD (2023), “06.02.2023 01:17:32 Pazarcık (Kahramanmaraş) earthquake M_w 7.7”, *Turkish Disaster and Emergency Management Presidency,* available in https://tadas.afad.gov.tr/event-detail/17966 .

Audemard FA (2006) “Surface rupture of the Cariaco July 09, 1997 earthquake on the El Pilar fault, northeastern Venezuela”, *Tectonophysics* **424**: 19–39.

Ahn J, Lešková A (2026) “Thirty-Nine Seconds: Insights from the 2026 Venezuela Earthquake.” *ALLATRA Natural Science Review* **1**: 34-44.

Apostolou M, Gazetas G, Garini E (2007) “Seismic Response of Simple Slender Structures with Foundation Uplifting”. *Soil Dynamics and Earthquake Engineering* **27**: 642-654.

Apostolou M (2011). *Soil–structure interaction under strong seismic moment: material and geometric nonlinearity*. Ph.D. Thesis, National Technical University of Athens, https://www.openarchives.gr/aggregator-openarchives/edm/phdtheses/000040-10442_38806

Baker WJ (2007). Quantitative classification of near fault ground motions using wavelet analysis, *Bulletin of the Seismological Society of America* **97**:1486–1501.

Beheshtian B, Somerville P (2026). “The 24 June 2026 Venezuela Earthquake Doublet”. *Briefing note 534. Insights, Risc Frontiers* : https://riskfrontiers.com/insights/the-24-june-2026-venezuela-earthquake-doublet/

Bernal G , Cardona OD (2026). “Strong Ground Motion Modeling of the Second Earthquake of June 24, 2026, in Venezuela” *An Exceptional Seismic Demand and its Implications for Earthquake-Resistant,* Ingeniar – Risk Intelligence report. www.ingeniar-risk.com.

Bertero VV, Mahin S, Herrera R (1978). “Aseismic design implications of near-fault San Fernando Earthquake records”. *Earthquake Engineering and Structural Dynamics* **6**(1): 31–42.

Bixel RA, Heydinger GJ, Guenther DA (2010), *Measured Vehicle Center-of-Gravity Locations — Including NHTSA's Data Through 2008 NCAP*. SAE Technical Paper: 2010-01-0086

Bustos J, Girmay N, Bravo-Haro M, Rojas R, Montemayor D, Heresi P, Miranda E, Pinto F, Montalva G, Bastías N, Ojeda J, Paz F, Villena F, Villegas A (2026) “Ground-Motion Intensity in Caraballeda During the 24 June 2026 Mw 7.5 Venezuela Earthquake Estimated from CCTV Video”, *The Seismic Record* **6**(4): 411–422.

Chaves EJ, Stein RS, Toda S (2026) “Venezuela’s Doublet Leaned Toward Caracas.” *Temblor,* https://temblor.net/earthquake-insights/venezuelas-doublet-leaned-toward-caracas-17281

Chrysler (2007). *2008 Jeep Liberty: Specifications*. Jeep Liberty Launch Kit, September 1, 2007. Chrysler LLC.

Colón S, Audemard FA, Beck C, Avila J, Padrón C, De Batist M, Paolini M, Leal AF, Van Welden A (2015) "The 1900 M_w 7.6 earthquake offshore north-central Venezuela: Is La Tortuga or San Sebastián the source fault?", *Marine and Petroleum Geology* **67**: 498-511.

Copernicus Emergency Management Service (CEMS): Earthquake in Venezuela, EMSR884 - Situational reporting, Copernicus EMS https://storymaps.arcgis.com/stories/717d0c07ec434b54ab6b2e0bbd7bc9f6

Czarnecki J (2008). *Final report of FMVSS 201 compliance testing of a 2008 Jeep Liberty Sport 4×4, NHTSA No. C80304*. Report No. 201UI-CAL-08-07, Calspan Test No. 8851-07. Calspan Transportation Sciences Center, Buffalo, NY. Prepared for the U.S. Department of Transportation, National Highway Traffic Safety Administration.

Daihatsu Terios (Second Generation, Model Code J200) Specifications: https://www.encycarpedia.com/daihatsu/08-terios-1-5-2wd-suv

Dewey J. W. (1972). "Seismicity and tectonics of western Venezuela". *Bulletin of the Seismological Society of America* **62**(6): 1711-1751.

Dudziak M, Lewandowski A, Waluś K J (2020). "Static tests the stiffness of car tires". *IOP Conference Series: Materials Science and Engineering* **776**: 012071.

Farazmand M, Behnamfar F, Aziminejad A (2025) "Seismic response of structures on flexible base under foundation uplift augmented by vertical component of near-field ground motions", *Soil Dynamics and Earthquake Engineering* **191**: 109278.

Fathi H, El-Sayegh Z, Ren J, El-Gindy M (2024) "Modeling and Validation of a Passenger Car Tire Using Finite Element Analysis", *Vehicles* **6**(1): 384-402.

Figini R, Paolucci R (2017) "Integrated foundation–structure seismic assessment through non-linear dynamic analyses". *Earthquake Engineering & Structural Dynamics* **46**(3): 349–367.

Gabor D. (1946) "Theory of communication. I. The analysis of information", *IEEE* **93**: 429–441.

Garini E, Gazetas G (2023) *Preliminary Report on the M_w7.8 and M_w7.5 earthquakes of February 6, 2023, in Turkey*, Report of Geo-Engineers Without Borders (GeoWB), ISSMGE, doi: 10.17605/OSF.IO/V4MSW

Garini E, Makris N, Gazetas G (2014) "Elastic and Inelastic Systems under Near-Fault Seismic Shaking: Acceleration Records Versus Optimally-Fitted Wavelets". *Bulletin of Earthquake Engineering*, doi: 10.1007/s10518-014-9631-z.

Garini E, Gazetas G, Anastasopoulos I (2017) "Evidence of significant forward rupture directivity aggravated by soil response in an M_w6 earthquake, and the effect on monuments", *Earthquake Engineering and Structural Dynamics* **46** (13): 2103–2120.

Garini E, Gazetas G (2013) “Damage Potential of Near-Fault Records: Sliding Displacement against Conventional “Intensity Measures”, *Bulletin of Earthquake Engineering* **11**: 455-480.

Gazetas G (1983) "Analysis of Machine Foundation Vibrations: State of the Art", *Soil Dynamics and Earthquake Engineering*, **2 (**1): 2 – 43.

Gazetas G, Garini E, Berill JB, Apostolou M (2012) “Sliding and Overturning Potential of the Christchurch 2011 Earthquake Records”, *Earthquake Engineering and Structural Dynamics* **41**(14): 1921-1944.

Gutierrez Soto M, Balderrama J, Brugés I, Cepeda J, Mejía M, Bektas N, Giannakogiorgos A, Caballero Calderón J, Romão X, Pereira J, Iturburu L, Hincapié J, Manco A, Ewis AA, Feinstein T, Napolitano R, et al (2026) “StEER: June 24 Venezuela Earthquake Sequence Annotated Media Repository”, *2026 Venezuela Earthquake Sequence*, *DesignSafe-CI*. https://doi.org/10.17603/ds2-v2w1-yj95.

Hall JF, Heaton TH, Halling MW, Wald DJ (1995) “Near-source ground motion and its effects on flexible buildings”, *Earthquake Spectra* **11**: 569–605.

Han Y, Lu Y, Liu J, and Zhang J (2022) “Research on Tire/Road Peak Friction Coefficient Estimation Considering Effective Contact Characteristics between Tire and Three-Dimensional Road Surface”, *Machines* **10**: 614.

Housner GW (1963) “The behavior of inverted pendulum structures during earthquakes”, *Bulletin of the Seismological Society of America* **53**(2):404–17.

Hairer E, Nørsett SP, and Wanner G (1993) *Solving Ordinary Differential Equations I: Non-stiff Problems*. 2nd Edition, Springer-Verlag (Publisher), Berlin, ISBN: 978-3-540-56670-0.

INGV (2026) *Earthquake with magnitude of Mw 7.5 on date 25-06-2026 and time 00:05:11 (Italy) Near coast of Venezuela*. *Istituto Nazionale di Geofisica e Vulcanologia*, Rome. https://terremoti.ingv.it/en/finitesource_summary/4588515 1

Jampole E, Miranda E, Deierlein GG (2018) “Predicting earthquake-induced sliding displacements using effective incremental ground velocity”, *Earthquake Spectra* **36** (1): 378–399, doi:10.1177/8755293019878200.

Lambourn R, Wesley A (2010) *"Motorcycle Tire/Road Friction"*. SAE 2010 World Congress & Exhibition, Detroit, Michigan, United States, https://doi.org/10.4271/2010-01-0054.

Larsen MC, Wieczorek GF, Eaton LS, Torres-Sierra H (2001) “Natural hazards on alluvial fans: the debris flow and flash flood disaster of December 1999, Vargas state, Venezuela”. Proceedings of the 6th Caribbean Islands Water Resources Congress, Mayagüez, Puerto Rico, W.F. Sylva (ed.).

Li D, Xiao B, Pan H (2022) “Estimating severe irregularities of road ahead based on preceding vehicle responses”. *Control Engineering Practice* **127**, doi:10.1016/j.conengprac.2022.105300.

Makris N, Black CJ (2004) “Dimensional analysis of rigid-plastic and elastoplastic structures under pulse-type excitations” *Journal of Engineering Mechanics* **130**(9):1006–1018.

Makris N, Roussos Y (2000) “Rocking response of rigid blocks under near source ground motions”. *Géotechnique* **50**(3):243–262.

Mangiagalli M, Ottaviani F, Alessandrini M, Menichetti M (2026) “The 24 June 2026 Earthquake Doublet in Northwestern Venezuela: Joint Hypocentral Determination, Fault-Zone Tomography and Four-Track Sentinel-1 Constraints on Rupture Geometry, Slip and Stress Transfer”. *Remote Sensing*: doi.org/10.3390/rs18193298

Mavroeidis DP, Papageorgiou AS (2008) “Near-fault ground motion and its relation to the fault rupture process”. *14th World Conference on Earthquake Engineering,* Beijing, China.

Mavroeidis DP, Papageorgiou AS (2003) “A mathematical representation of near fault ground motions”. *Bulletin of the Seismological Society of America* **93**(3): 1099–1131.

Merritt DK, Lyon CA, Persaud BN (2015) “Evaluation of Pavement Safety Performance”. U.S. Department of Transportation, Federal Highway Administration, Research Publication, Publication Number: FHWA-HRT-14-065

Miyazaki M, Nishimura Y, Mizue T (2023). *“Practice of 100-kine damage-free design: A record of challenges to near-field ground motions from the Kobe earthquake” (in Japanese). Japan Society of Seismic Isolation (ed.) JSSI 30th Anniversary Commemorative History: Seismic Isolation and Vibration Control - Tracks of Challengers, dynamic-d.co.jp*

op het Veld, IBA (2008). “*Enhancing the MF-Swift Tyre Model for Inflation Pressure Changes”*. Master's thesis, Department of Mechanical Engineering, Eindhoven University of Technology, The Netherlands.

Pérez O J, Bilham R, Bendick R, Velandia J R, Hernández N, Moncayo C, Hoyer M, & Kozuch M (2001). “Velocity field across the Southern Caribbean Plate Boundary and estimates of Caribbean/South-American Plate Motion using GPS Geodesy 1994–2000”. *Geophysical Research Letters* **28**(15): 2987–2990.

Pousse Beltran L, Pathier E, Jouanne F, Vassallo R, Reinoza C, Audemard F, Doin M P, & Volat M. (2016). “Spatial and temporal variations in creep rate along the El Pilar fault at the Caribbean-South American plate boundary (Venezuela), from InSAR”. *Journal of Geophysical Research: Solid Earth* **12**1(11): 8276–8296.

Restrepo J et al (2026) “Topic 2: Preliminary Interpretation of On-the-Fault Pulse of the 2026 Mw 7.5 Venezuela Earthquake”. Oral presentation, 8th Kenji Ishihara Colloquium, EERI, San Diego, September 2026.

Riquelme S, Crempien JGF, Koch P, Bravo F., Benavente R, Toledo PA, Rocabado V, Schmitz M, Alvarado L, Lopez R, and Barrientos S (2026) “The 24 June 2026 Venezuela Earthquake Sequence: A Multi-fault M_w 7.6 Supershear Rupture on the Boconó and San Sebastián Faults Constrained by Near- and Far-Field Observations”, *The Seismic Record* **6**(4): 433–442.

Sadauckas J, Schoeneck N, Nagurka M (2025) “Radial stiffness and damping of mountain bike tires subject to impact determined using the coefficient of restitution”. *Vehicle System Dynamics* **63**(10):1962–1982.

Sassani M, Bertero VV (2002) “Importance of severe pulse-type ground motions in performance-based engineering: historical and critical review”, *Proceedings of the 12th World Conference on Earthquake Engineering*, R. Park editor, New Zealand.

Schubert C (1984) "Basin formation along the Bocono-Moron-El Pilar Fault System, Venezuela", *Journal of Geophysical Research: Solid Earth* **89**(B7): 5711–5718.

Seed HB, Whitman RV, Dezfulian H, Dobry R, Idriss IM, Fuller FM (1972) "Soil Conditions and Building Damage in 1967 Caracas Earthquake", *Journal of Soil Mechanics and Foundations Division* **98** (SM8): 787- 806.

Soica A, Gheorghe C (2025) “Tire–Road Interaction: A Comprehensive Review of Friction Mechanisms, Influencing Factors, and Future Challenges”, *Machines* **13**: 1005.

Sokos E, Kiratzi A, Zahradnik J, Serpetsidaki A, Plicka V, Jansky J, Kostelecky J, Tselentis GA. (2015) “Rupture process of the 2014 Cephalonia, Greece, earthquake doublet (Mw6) as inferred from regional and local seismic data”, *Tectonophysics* **656**:131–141.

Somerville P, Graves R (1993) “Conditions that give rise to unusually large long period ground motions”, *Structural Design Tall Buildings* **2**: 211–232.

Somerville P (2000) “Seismic hazard evaluation”, *Bulletin of the New Zealand Society of Earthquake Engineering* **33**: 325–346 and 484–491.

Somerville PG, Smith NF, Graves R W, Abrahamson NA (1997) “ Modification of empirical strong ground motion attenuation relations to include the amplitude and duration effects of rupture directivity”, *Seismological Research Letters* **68** (1): 199–222

Tsopelas P, Constantinou MC, Kim YS, Okamoto S (1996), “Experimental study of FPS system in bridge seismic isolation”, *Earthquake Engineering and Structural Dynamics* **25**(1): 65–78.

United Nations Satellite Centre (UNOSAT): M 7.2 & 7.5 - Caracas Earthquake (24 June 2026 at 22:05:11 UTC) UNOSAT Analysis, https://arcg.is/1XfiOL1

USGS (2026) “M 7.5 - 20 km W of Catia La Mar, Venezuela”, *ANSS Comprehensive Earthquake Catalog*. US Geological Survey Earthquake Hazards Program. https://earthquake.usgs.gov/earthquakes/eventpage/us6000t7zp/executive

Vassiliou MF, Makris N (2011) “Estimating Time Scales and Length Scales in Pulse-like Earthquake Acceleration Records with Wavelet Analysis”, *Bulletin of the Seismological Society of America* **101**(2):596–618.

Virtanen P, Gommers R, Oliphant TE, Haberland M, Reddy T, Cournapeau D, Burovski E, Peterson P, Weckesser W, Bright J, van der Walt S J, Brett M, Wilson J, Millman K J, Mayorov , Nelson ARJ, Jones E, Kern R. Larson E, Carey C J, Polat , Feng Y, Moore EW, Vander Plas J, Laxalde D, Perktold J, Cimrman R, Henriksen I, Quintero EA, Harris CR, Archibald AM, Ribeiro AH, Pedregosa F, van Mulbregt P, SciPy 1. 0 Contributors (2020) "SciPy 1.0: fundamental algorithms for scientific computing in Python". *Nature Methods* **17**: 261-272.

Wong JWC, Bruck ER, Gonzalez RG, Marchandon M, Wu B, Kutschera F, Zebker M, Magen Y, Fan W, Fialko Y, Gabriel AA (2026) "Fitful but sustained rupture of the 2026 M_w7.6 Venezuela earthquake", *EarthArXiv Repository* (ID: 15594), https://eartharxiv.org/repository/view/15594/

Zimmerman MT, Shen-Tu, Shabestari K, Mahdyiar M (2023) "A comprehensive hazard assessment of the Caribbean region", *Bulletin of the Seismological Society of America* **113**(1): 667–696.

Zheng M, Peng P, Zhang B, Zhang N, Wang L, and Chen Y (2015) "A New Physical Parameter Identification Method for Two-Axis On-Road Vehicles: Simulation and Experiment", *Shock and Vibration* **2015**: ID 191050.

Zhu Y, Wang Y, and Huang Y (2014) "Failure analysis of a helical compression spring for a heavy vehicle's suspension system", *Case Studies in Engineering Failure Analysis* **2**: 169–173.

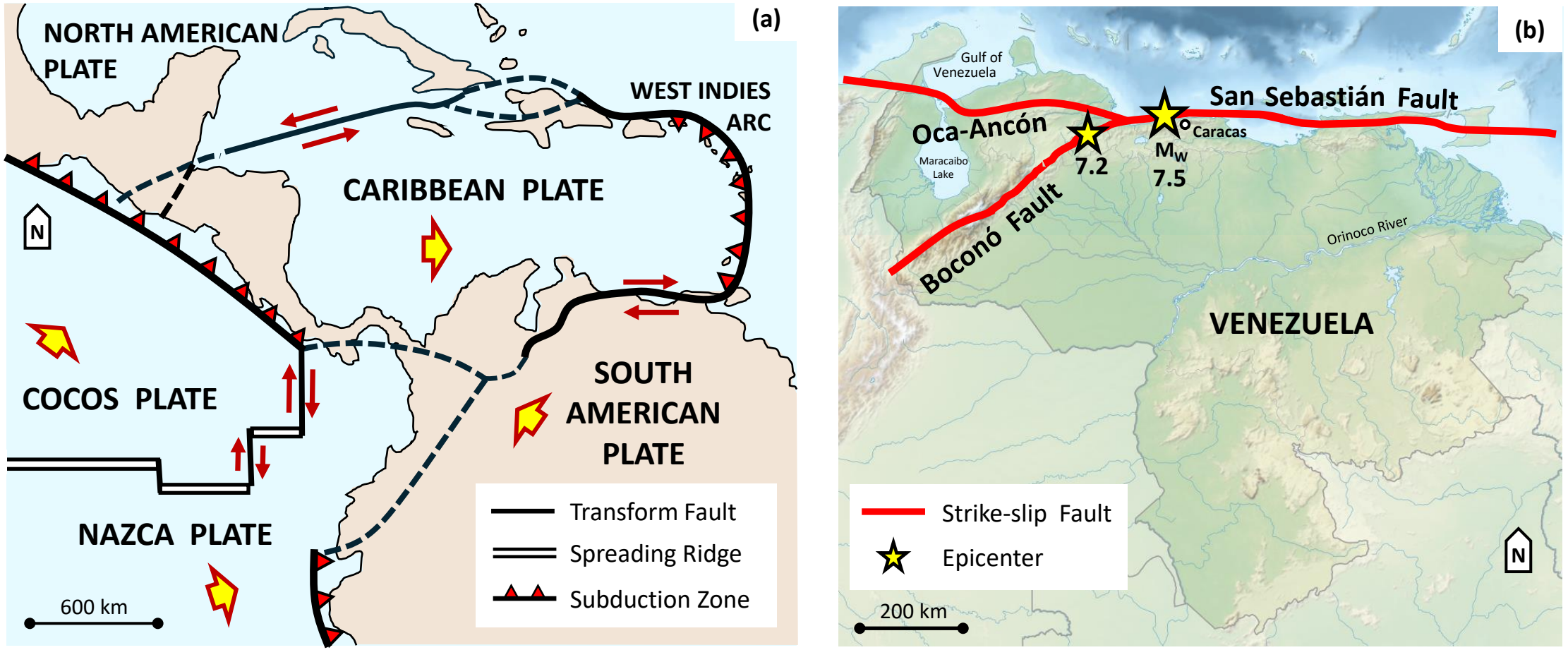


FIGURE 1 **(a)** The complex tectonic plate setting at the vicinity of Venezuela; **(b)** Main active faults and epicenters of the June 24th, 2026 earthquake doublet. (Modified map by Guiana_shield_map-fr.svg: CC BY 4.0, https://commons.wikimedia.org/w/index.php?curid=149631951).

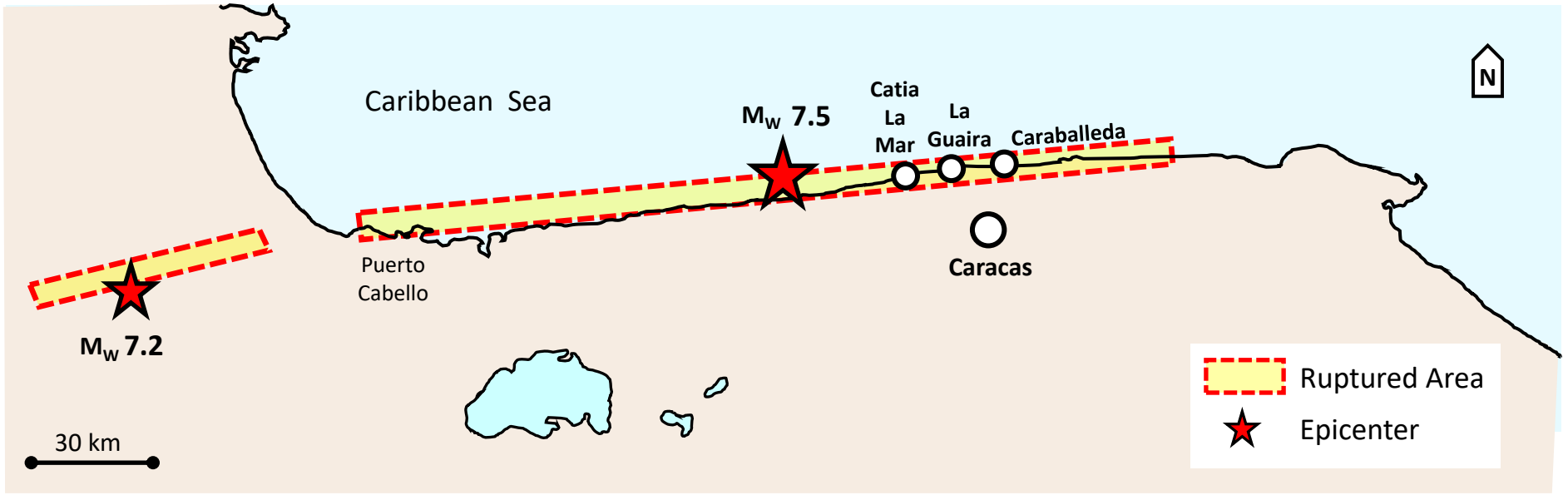


FIGURE 2 Epicenters and fault areas ruptured during the M_w7.2 and M_w 7.5 events of June 24th in Venezuela. [Data of the fault rupture models taken from USGS 2026].



FIGURE 3 Seismic structural damage map of part of Caraballeda, extracted from the United Nations Satellite Centre (UNOSAT) and Copernicus EMS and SERTIT [Source: https://arcg.is/1XfiOL1]

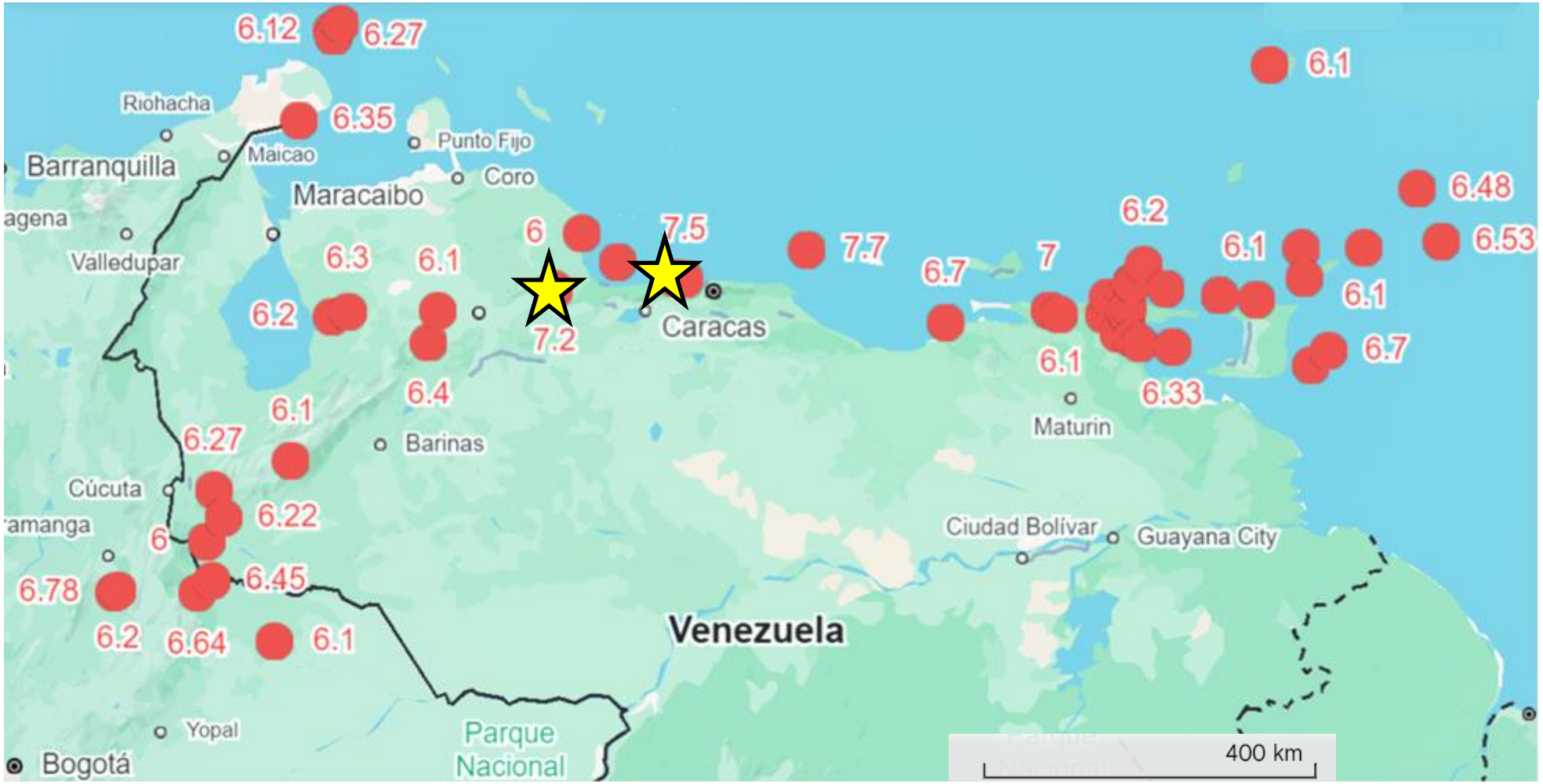


FIGURE 4 Major earthquakes (M ≥ 6.0) in Venezuela between 1900 and 2026, highlighting the June 24, 2026, seismic sequence in yellow stars. Earthquake epicenter locations and magnitudes are based on the USGS ANSS Comprehensive Earthquake Catalog (ComCat). Basemap: Google Earth.

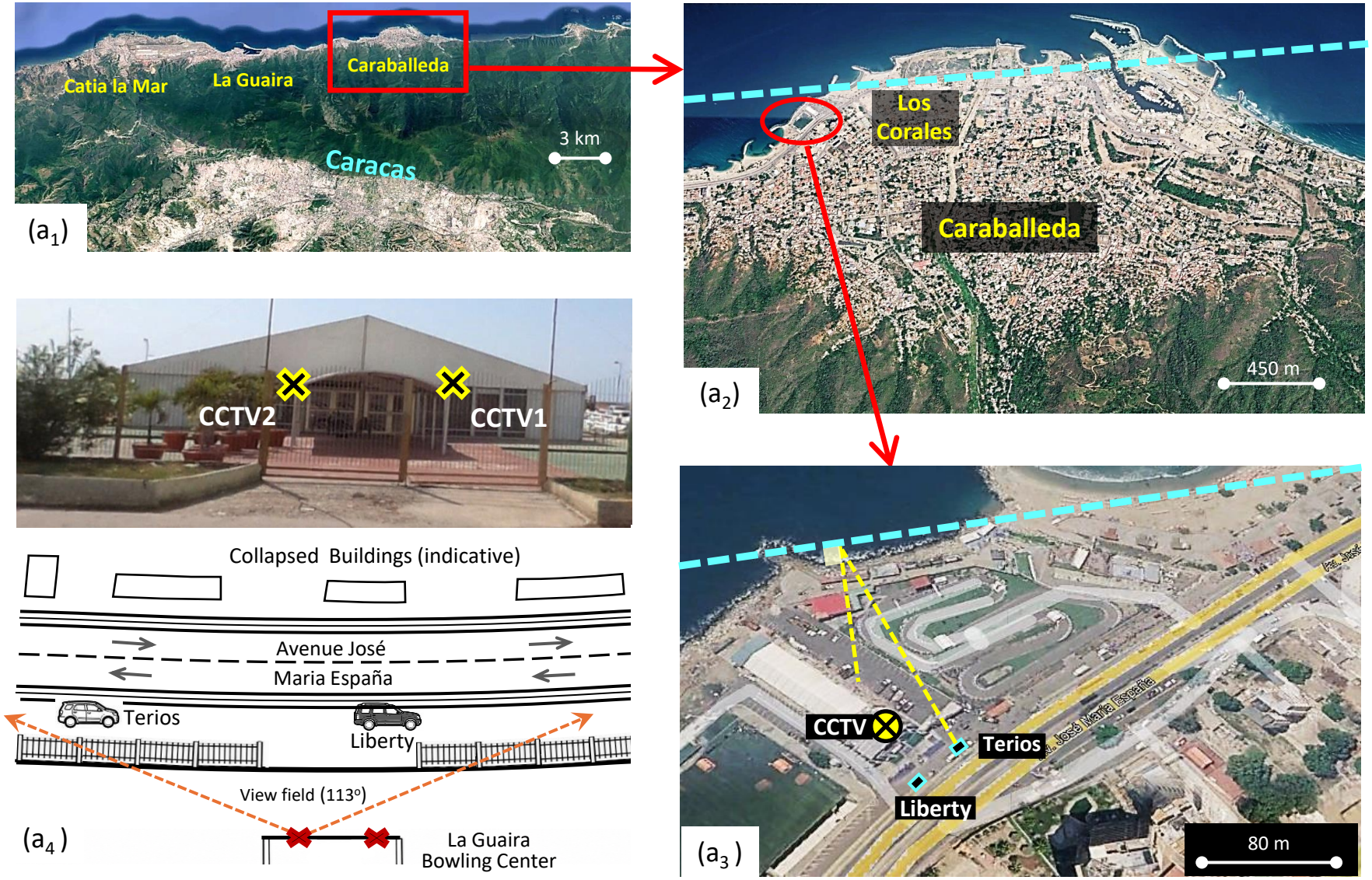


FIGURE 5 **(a_1)** Plan view of Caracas and the coastal cities most devastated on 24 June 26; **(a_2)** Caraballeda and seismogenic fault projection (dashed line); **(a_3)** Area of interest with the exact location of the building with the CCTV cameras and the two vehicles captured in motion and studied here; the thin dotted lines indicate the directions normal to the side of the Terios car and normal to the fault; **(a_4)** Front view of the sports building with the cameras, and sketch of the plan of the viewed area. Basemap: Google Earth.

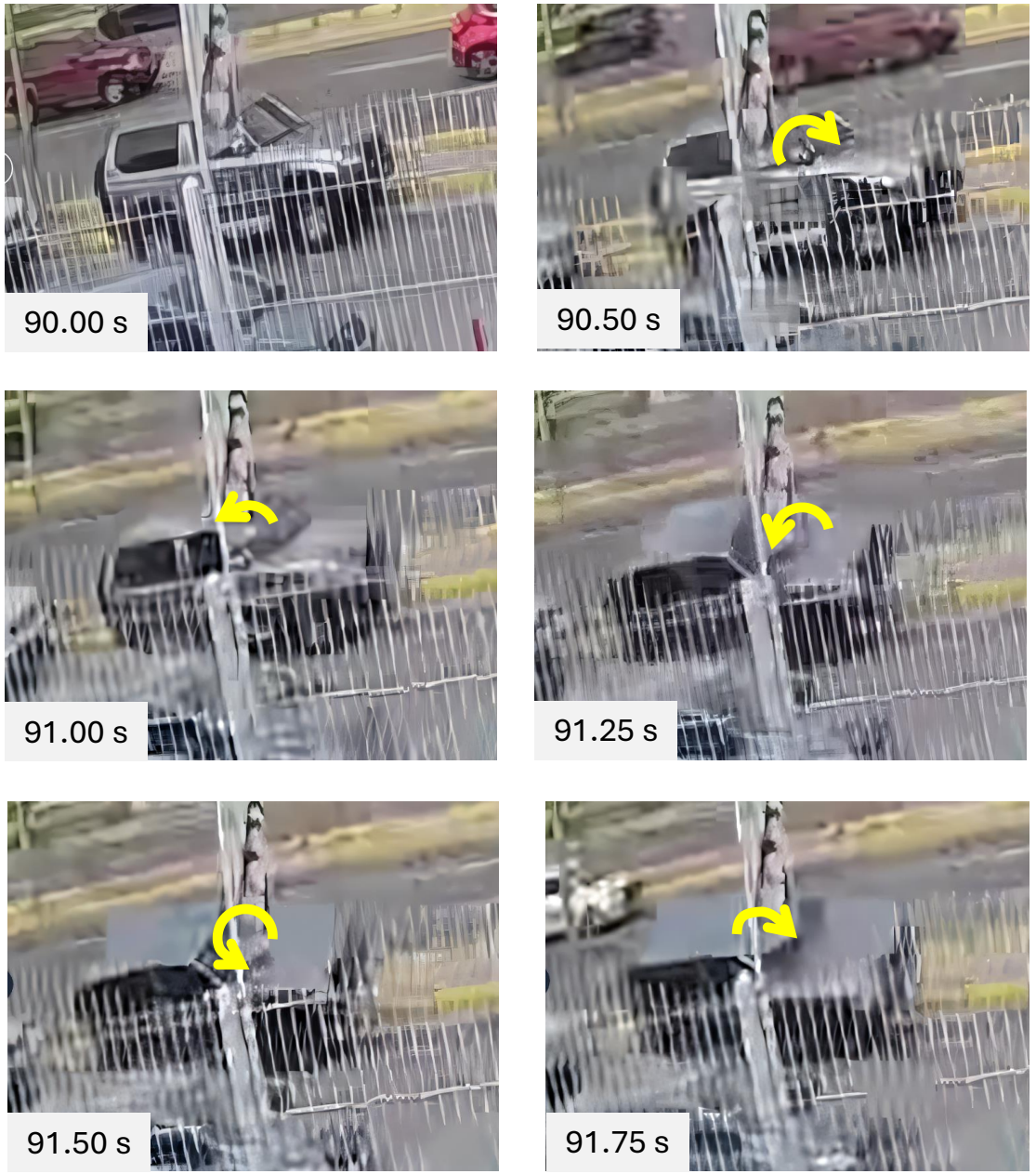


FIGURE 6 Selected snapshots of the oscillation of the Daihatsu Terios SUV car

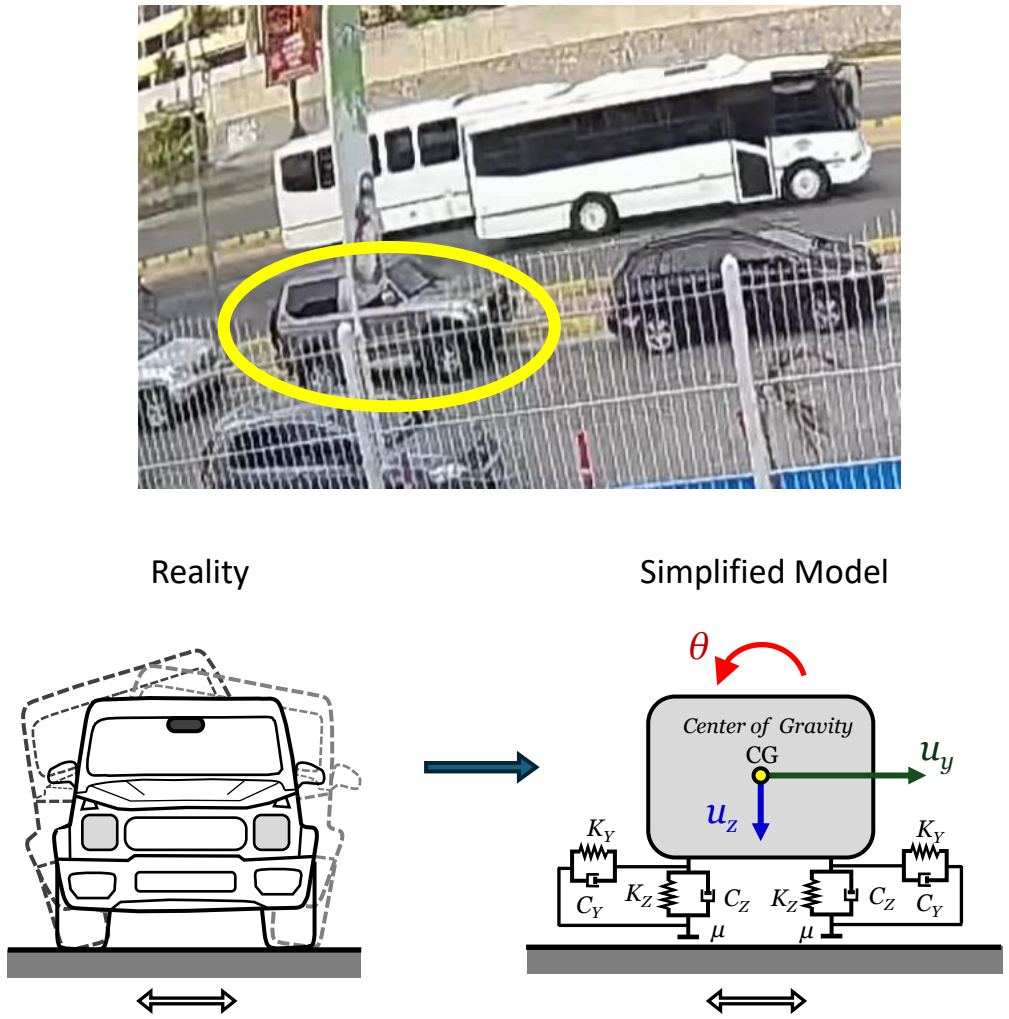


FIGURE 7 Photo of the Daihatsu Terios car, schematic representation of its lateral vibration, and the modelling on spring and dashpots, resting on the ground through Coulomb friction

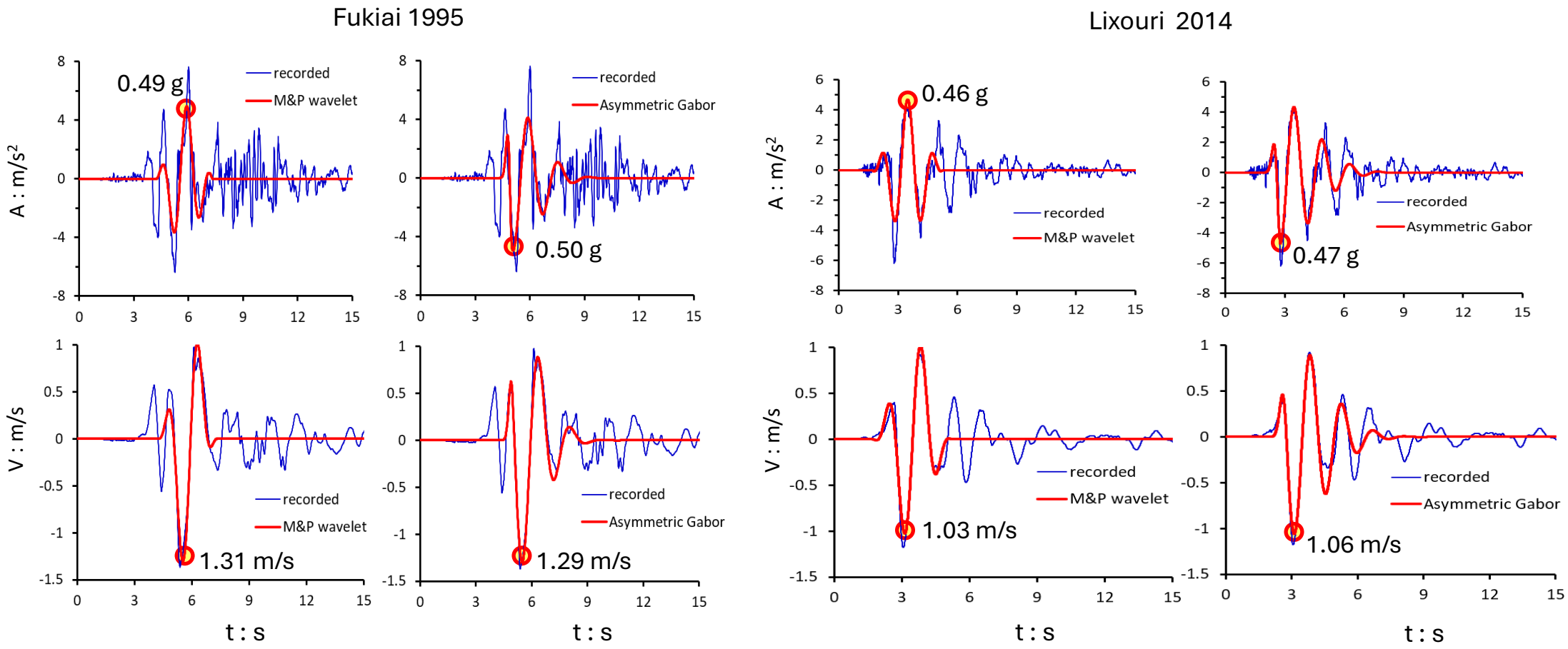


FIGURE 8 Acceleration and velocity time histories from the accelerograms Fukiai EW (in the Kobe 1995 earthquake) and Lixouri EW (in the Cephalonia 2014 earthquake) fitted with a Mavroeidis & Papageorgiou and with an asymmetric Gabor wavelet.

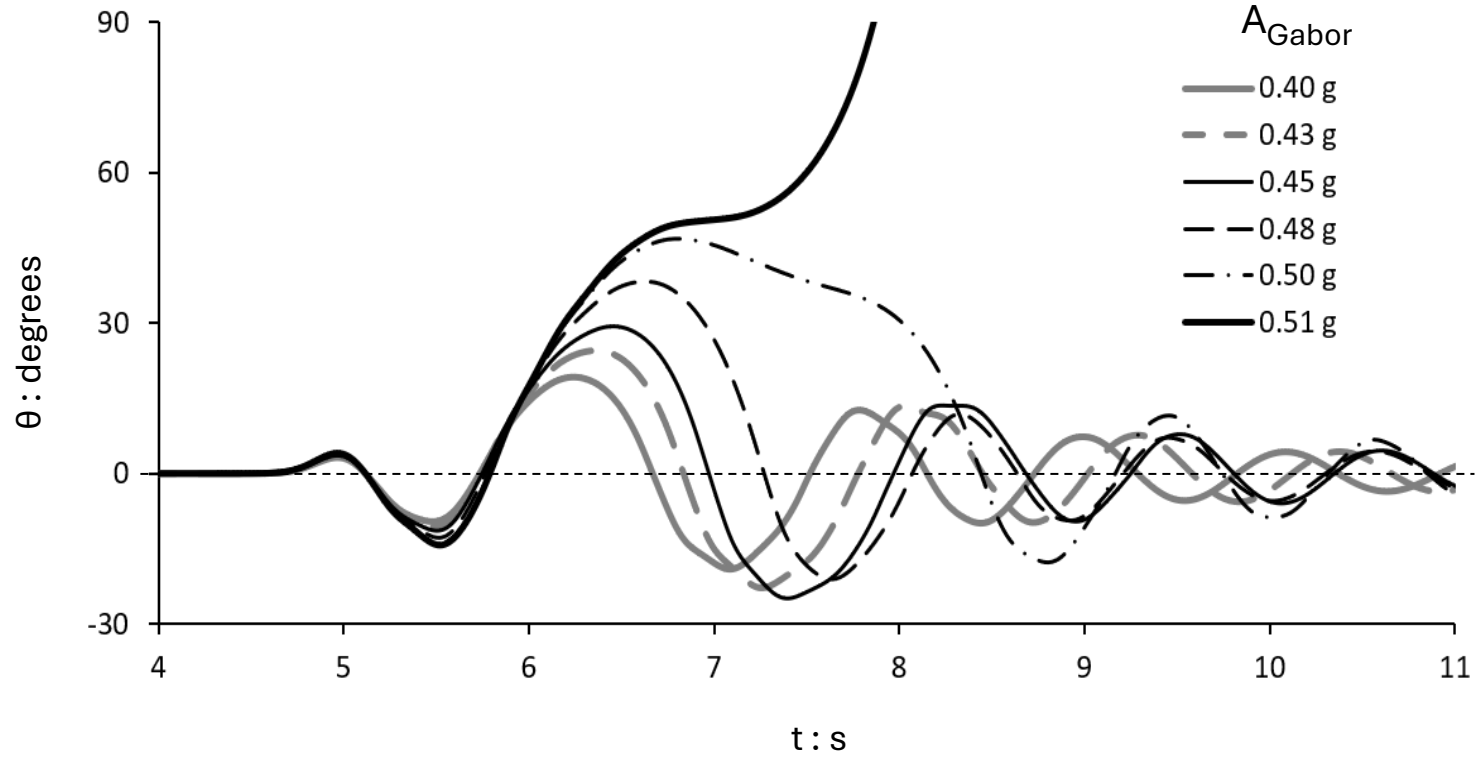


FIGURE 9 Comparative summary graph of the (total) rotation angle, $\theta(t)$, of the Daihatsu Terios car, due to **Fukiai-based** asymmetric **Gabor** wavelet with parametrically varying amplitudes, designated in terms of A_{Gabor}

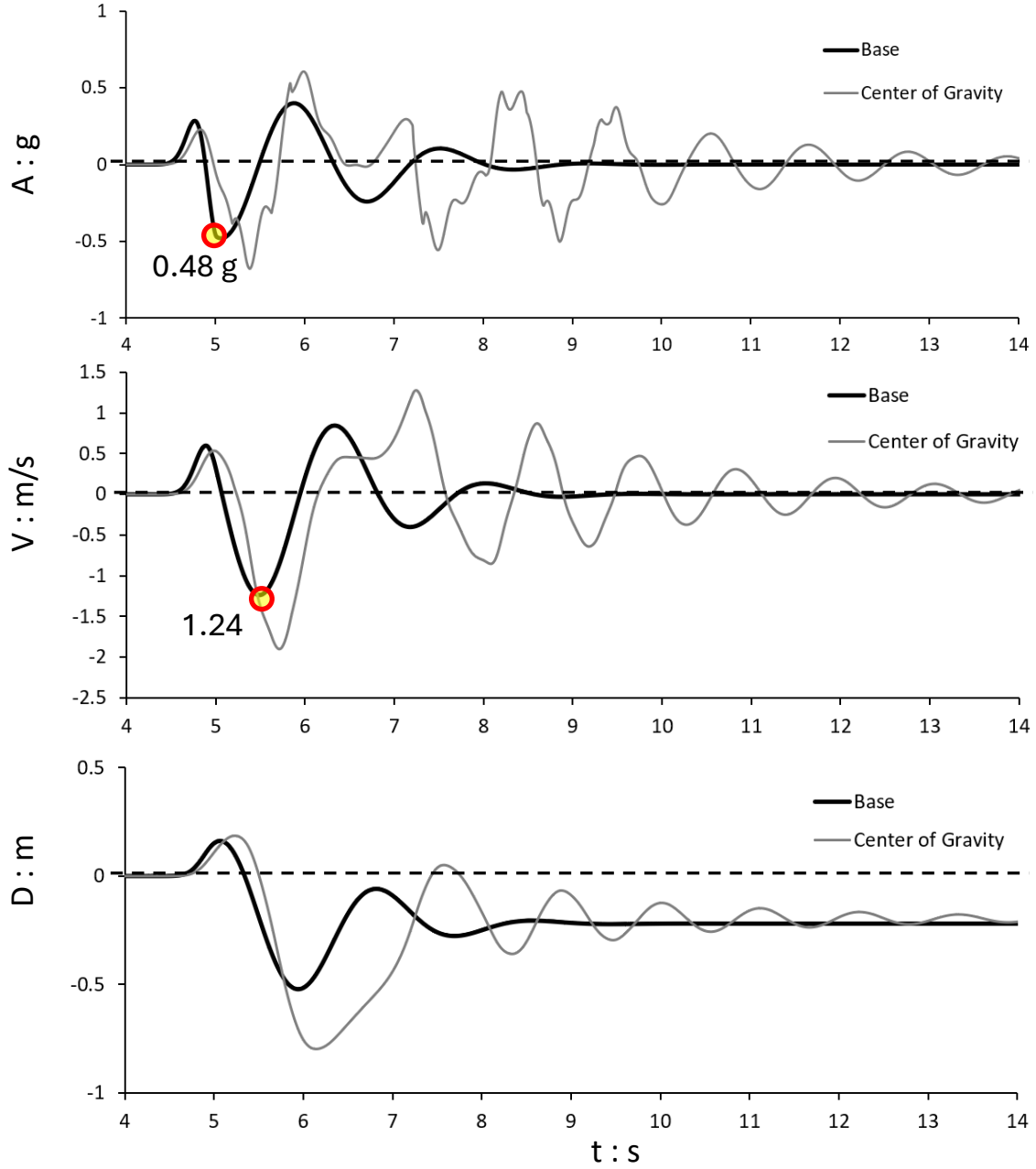


FIGURE 10. Acceleration, velocity and displacement time histories of the base and the Daihatsu Terios center of mass, due to the Fukiai based asymmetric Gabor wavelet down-scaled to A_{Gabor} **=0. 48 g,** V_{Gabor} **= 1.24 m/s** .

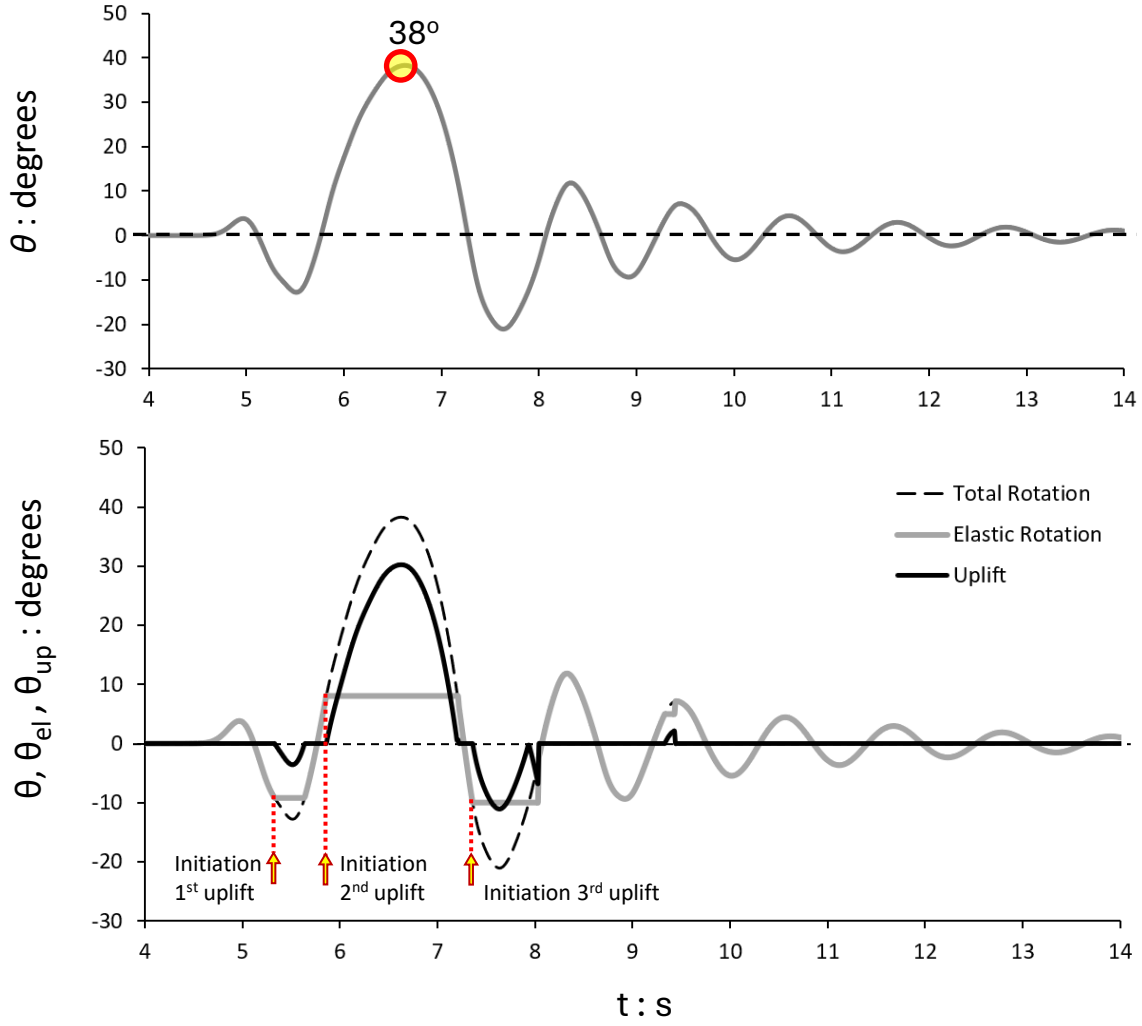


FIGURE 11 Rotational components of Daihatsu Terios car, due to the Fukiai based asymmetric Gabor wavelet down-scaled to A_{Gabor} =**0. 48 g,** V_{Gabor} = **1.24 m/s** . Notice that uplifting starts at the time when the elastic angle becomes constant (indicated by the red dotted lines).

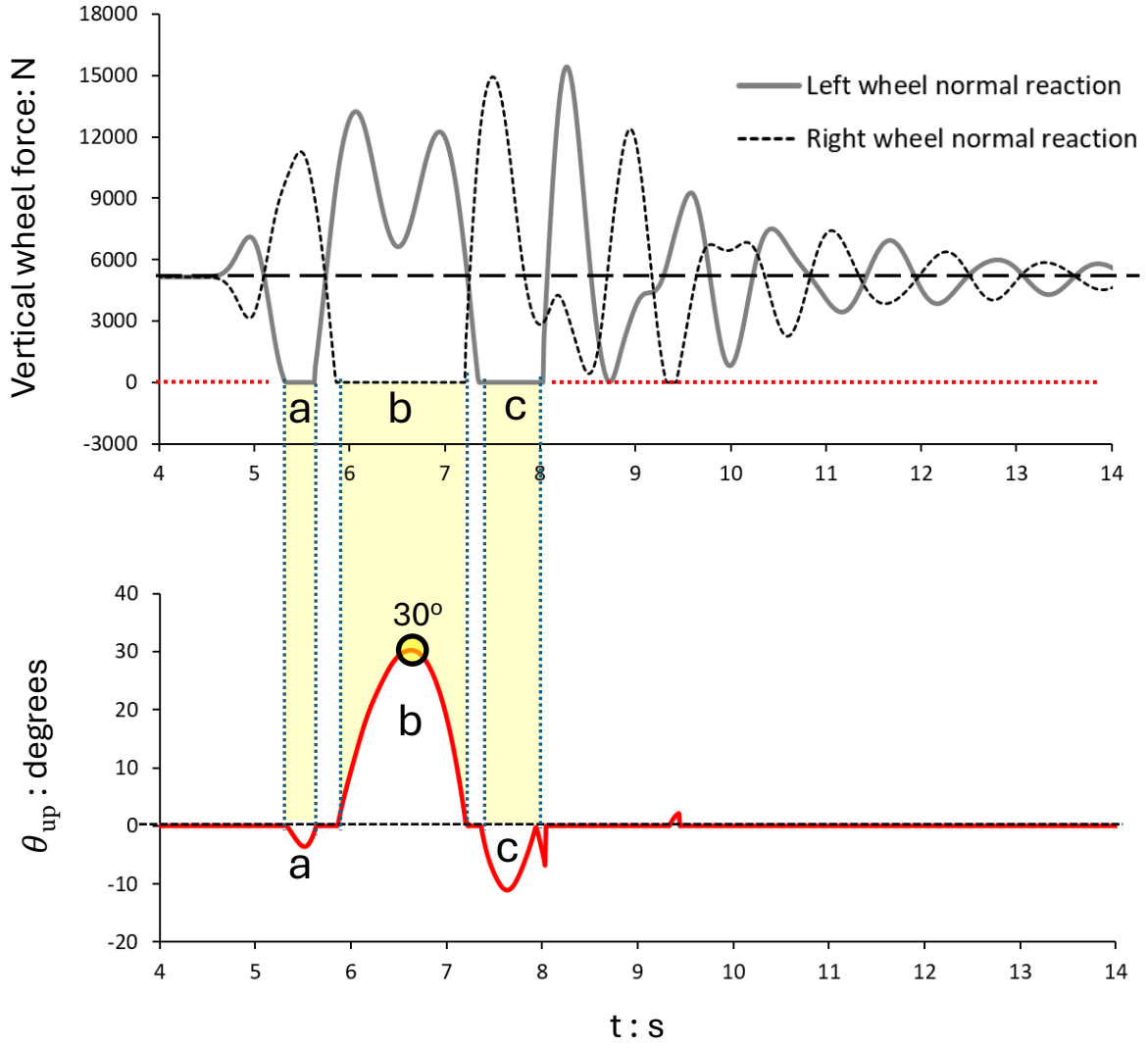


FIGURE 12 Uplifting angle $\theta_{up}(t)$ contrasted to the vertical reactions N(t) on the left- and right-side wheels of the Daihatsu Terios car, due to the Fukiai based asymmetric Gabor wavelet down-scaled to A_{Gabor} **=0. 48 g, V_{Gabor} = 1.24 m/s** .

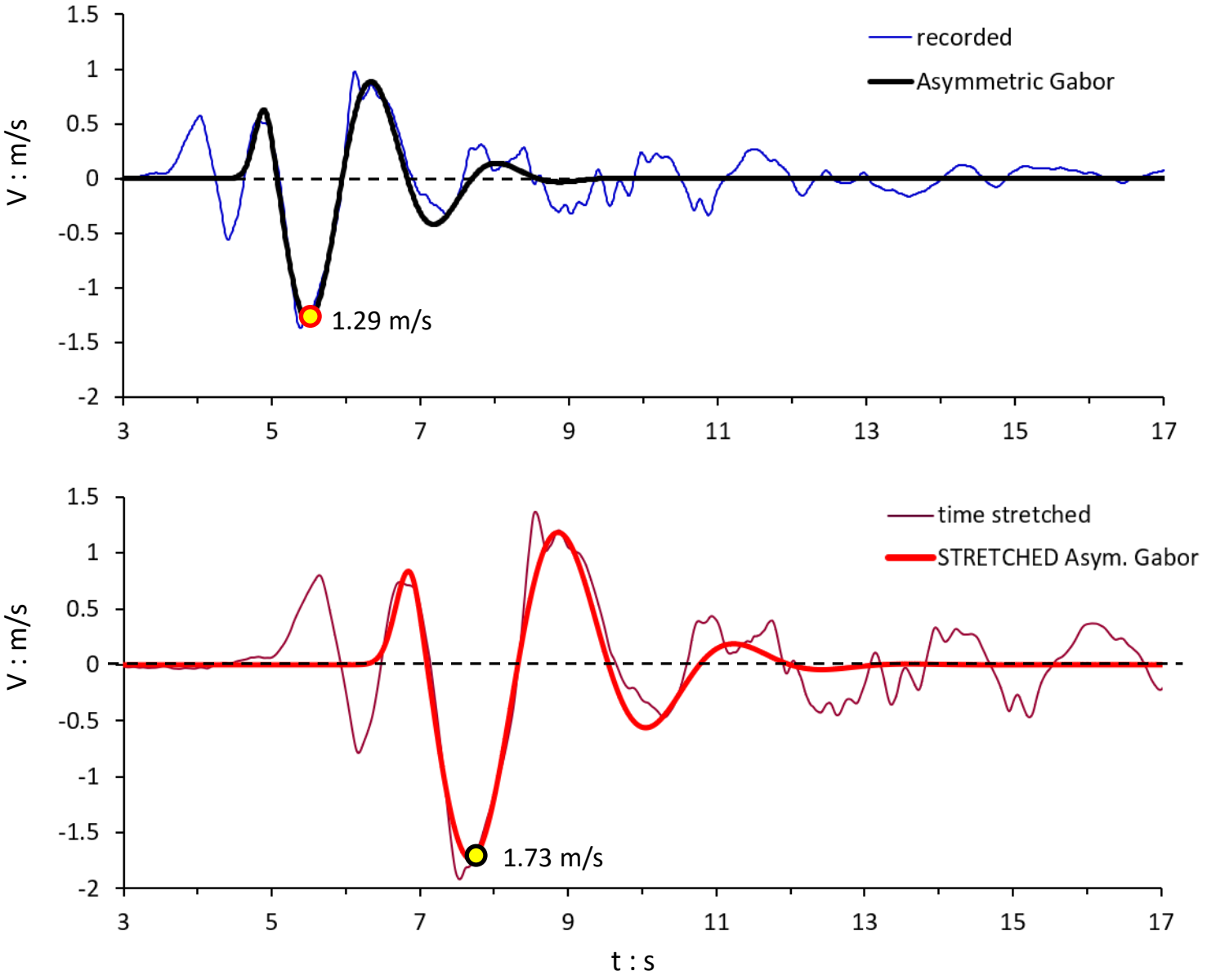


FIGURE 13 Velocity time histories of the recorded Fukiai motion and **the fitted asymmetric Gabor wavelet** in black (top), and **the time-stretched** Fukiai motion and its fitted wavelet in red (bottom).

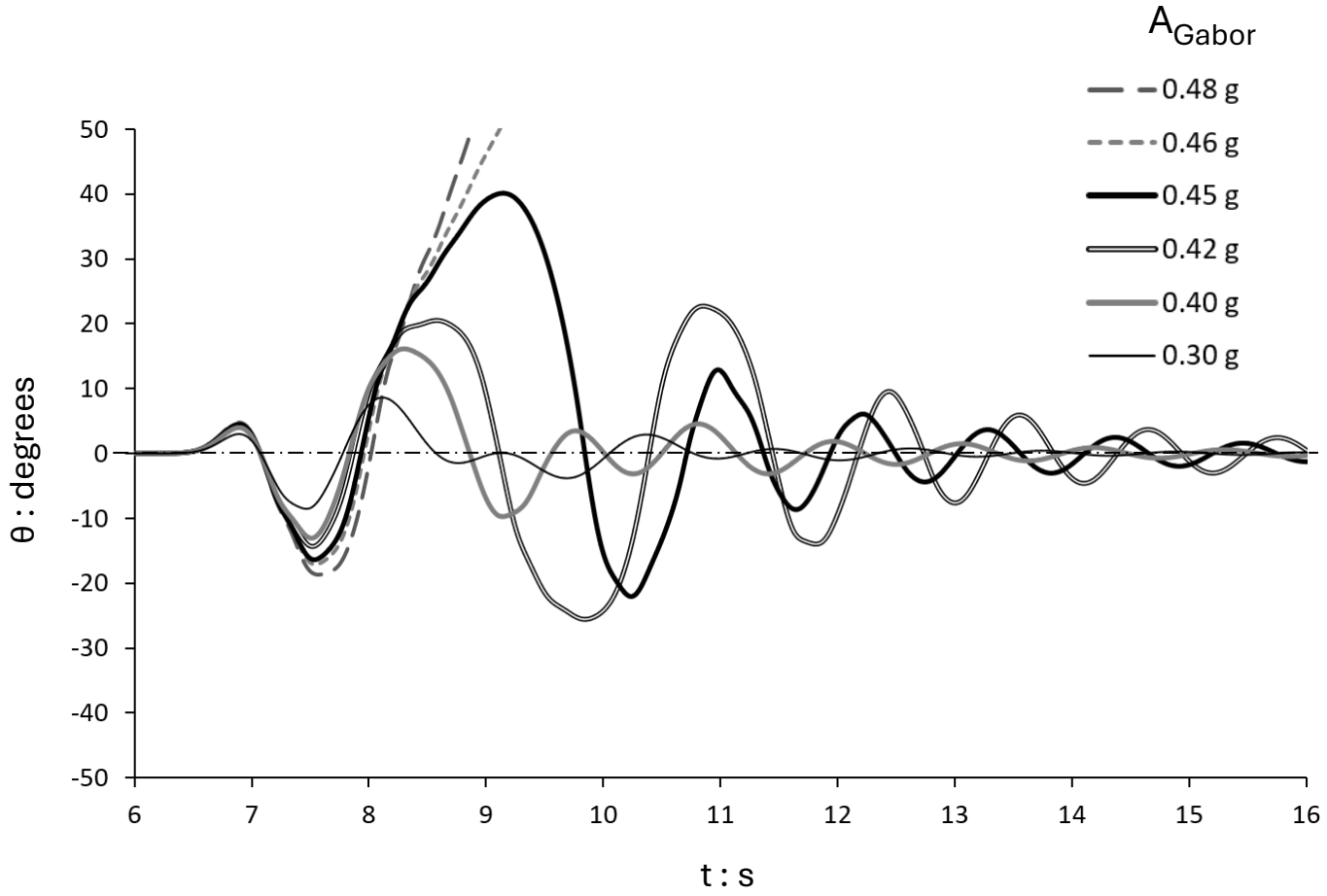


FIGURE 14 Comparative summary graph of the (total) rotation angle, $\theta(t)$, of the Daihatsu Terios car, due to the asymmetric **Gabor** wavelet fitted to the **time-stretched** Fukiai **motion,** with parametrically varying amplitudes, designated in terms of A_{Gabor}. The value $A_{Gabor} = 0.45$ g and correspondingly $V_{Gabor} = 1.60$ m/s are nearly optimum ($\theta \approx 40^{o}$).

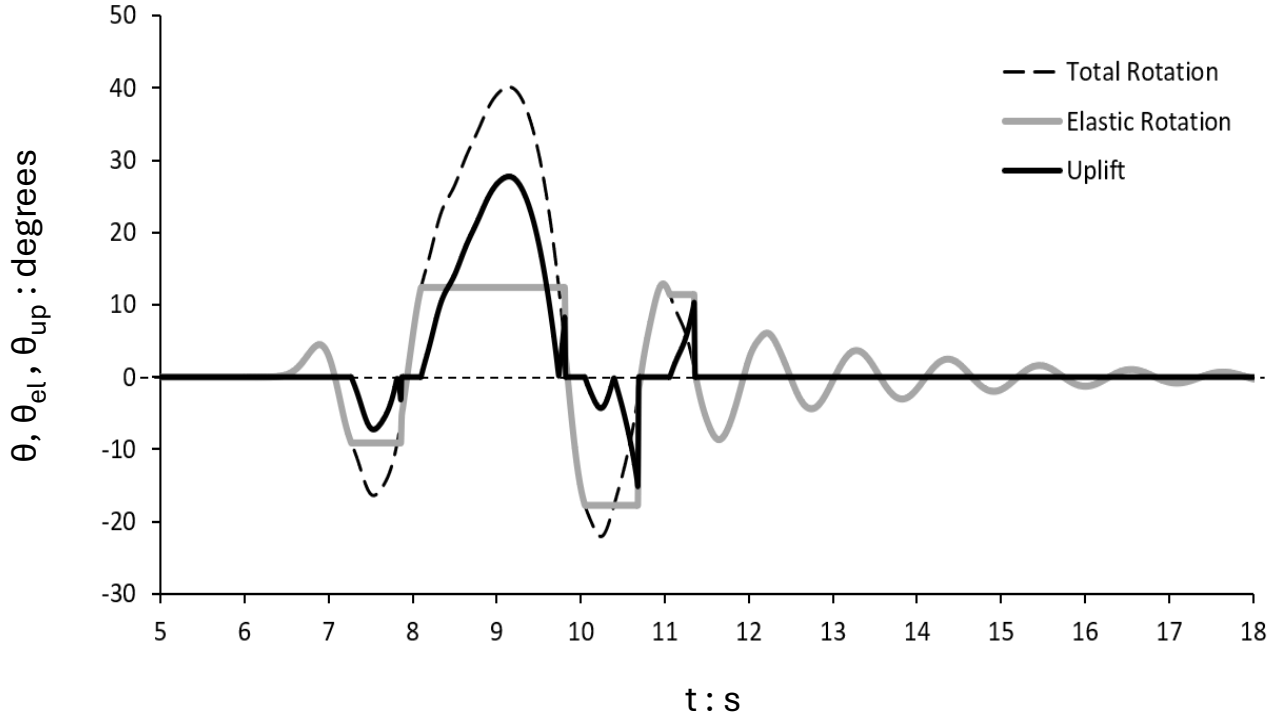


FIGURE 15 Angle of rotation time histories of the Daihatsu Terios car due to asymmetric Gabor pulse fitted to **time-stretched Fukiai** motion down-scaled to (A_{Gabor} = 0. 45 g, V_{Gabor} = 1.60 m/s) , and leading to $\theta \approx 40^{o}$, nearly as recorded.

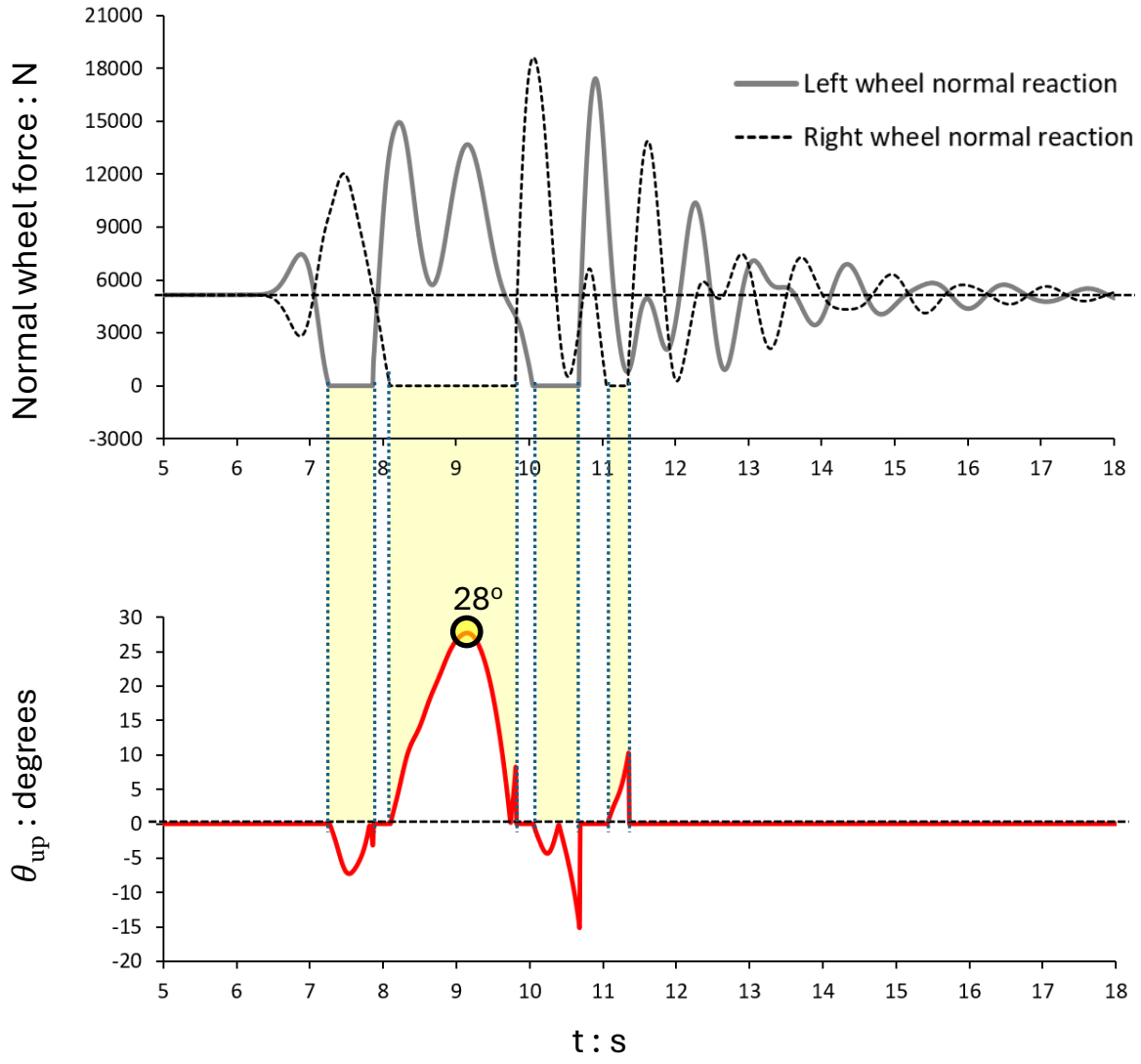


FIGURE 16 Uplifting angle θ_{up}(t) contrasted to the vertical reactions N(t) on the left- and right-side wheels of the Daihatsu Terios car, due to asymmetric Gabor pulse fitted to **time-stretched Fukiai** motion down-scaled to (A_{Gabor} = 0. 45 g, V_{Gabor} = 1.60 m/s).

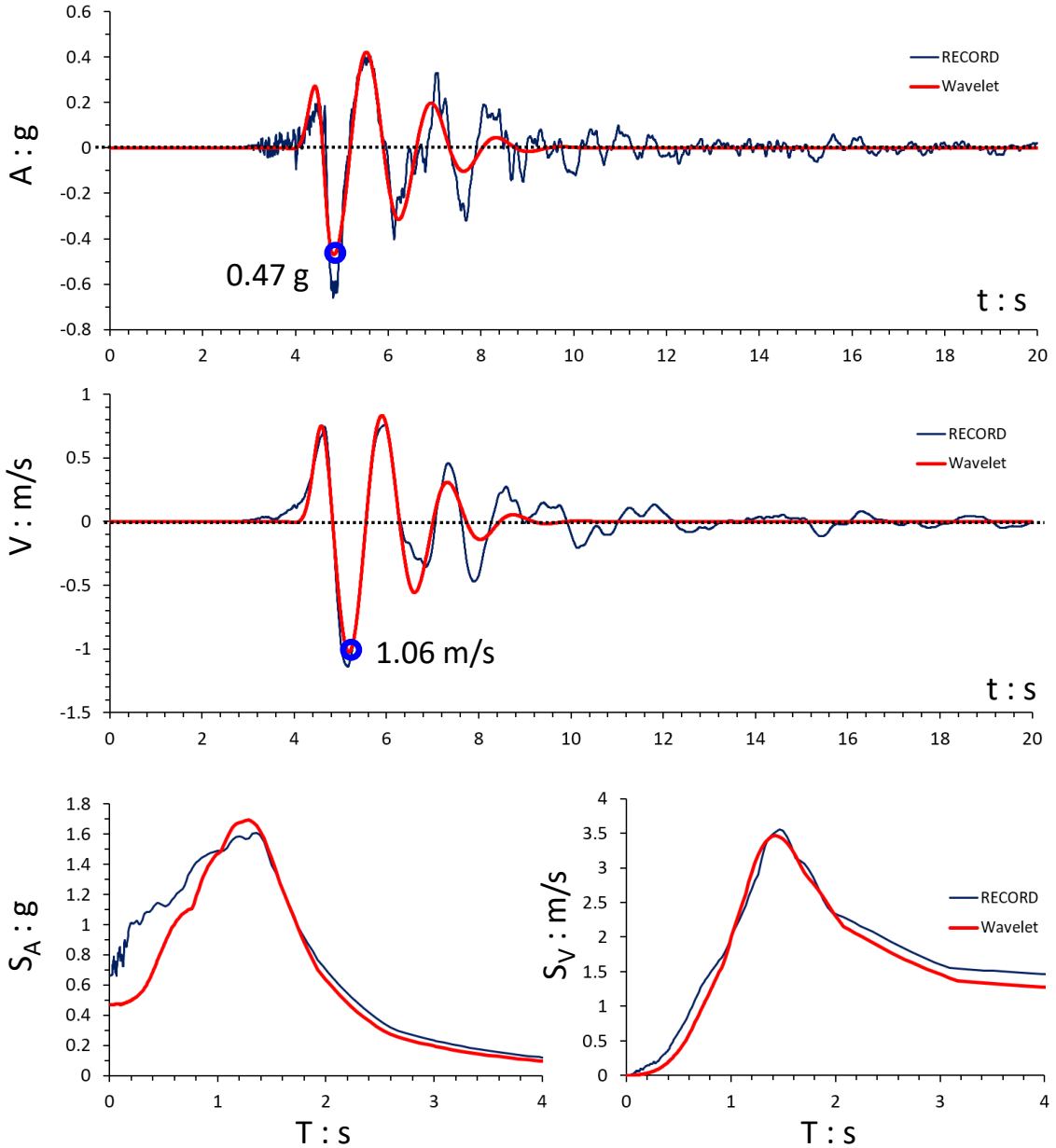


FIGURE 17 The recorded fault normal (EW component) **of Lixouri record** optimally fitted with asymmetric **Gabor wavelet** and their response spectra.

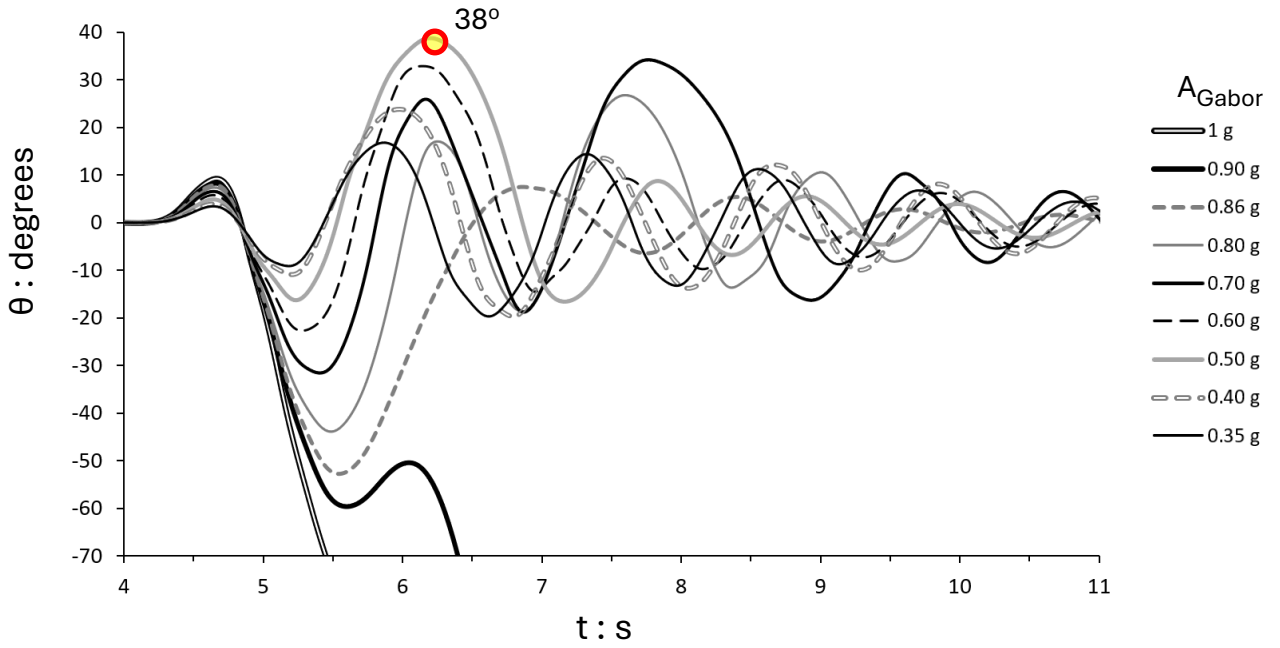


FIGURE 18 Comparative summary graph of the (total) rotation angle, $\theta(t)$, of the Daihatsu Terios car due to **Lixouri-based** asymmetric **Gabor** wavelet with parametrically varying amplitudes, designated in terms of A_{Gabor}. The value that corresponds to 38° is **0.50 g** with corresponding velocity **1.2 m/s**.

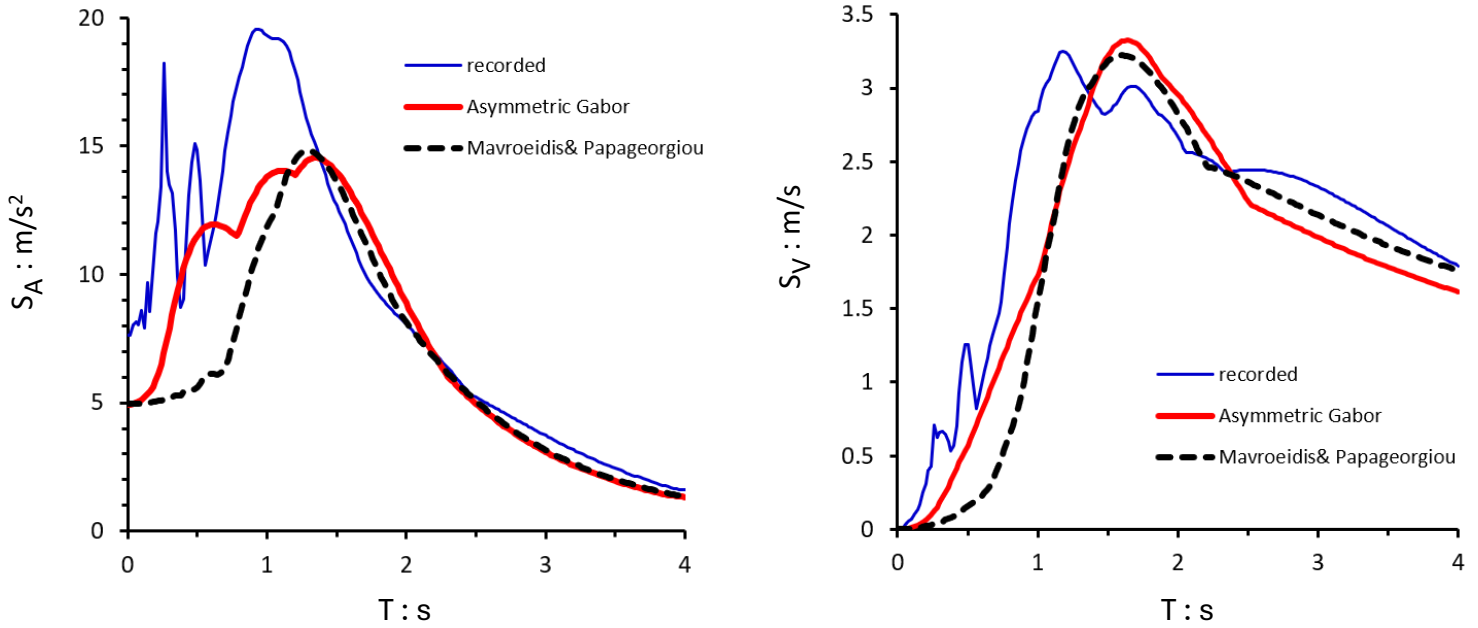


FIGURE 19 Acceleration and velocity elastic response spectra of Fukiai (as recorded with blue), the fitted asymmetric Gabor wavelet (in red) and the M&P wavelet (in dashed black).

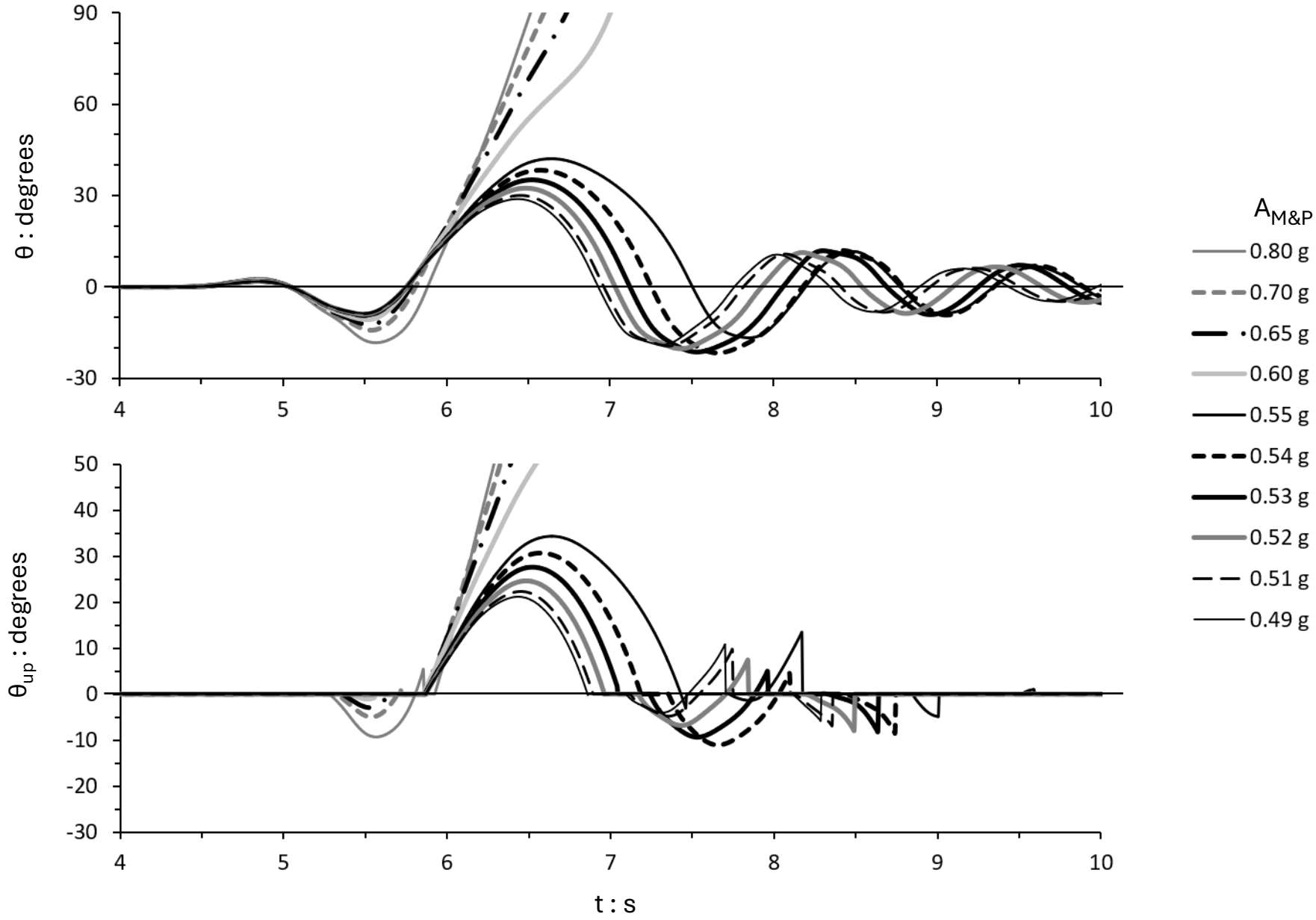


FIGURE 20 Comparative summary graph of the (total) rotation angle, $\theta(t)$, and the uplift rotation angle, $\theta_{up}(t)$, of the Daihatsu Terios due to **Fukiai-based** fitted **M&P** wavelet with parametrically varying amplitudes, designated in terms of $A_{M\&P}$

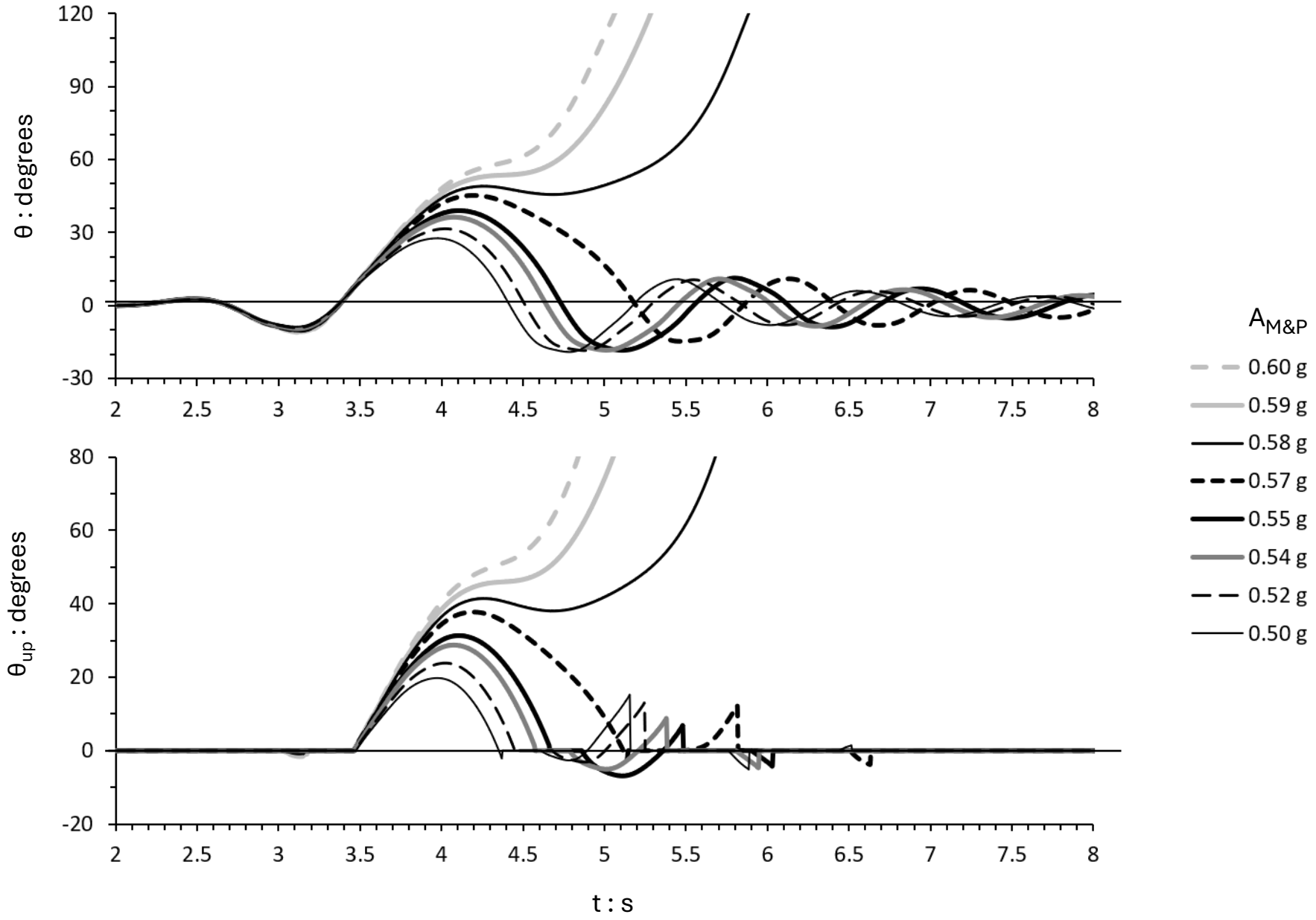


FIGURE 21 Comparative summary graph of the (total) rotation angle, $\theta(t)$, and the uplift rotation angle, $\theta_{up}(t)$, of the Daihatsu Terios due to **Lixouri-based** fitted **M&P** wavelet with parametrically varying amplitudes, designated in terms of $A_{M\&P}$

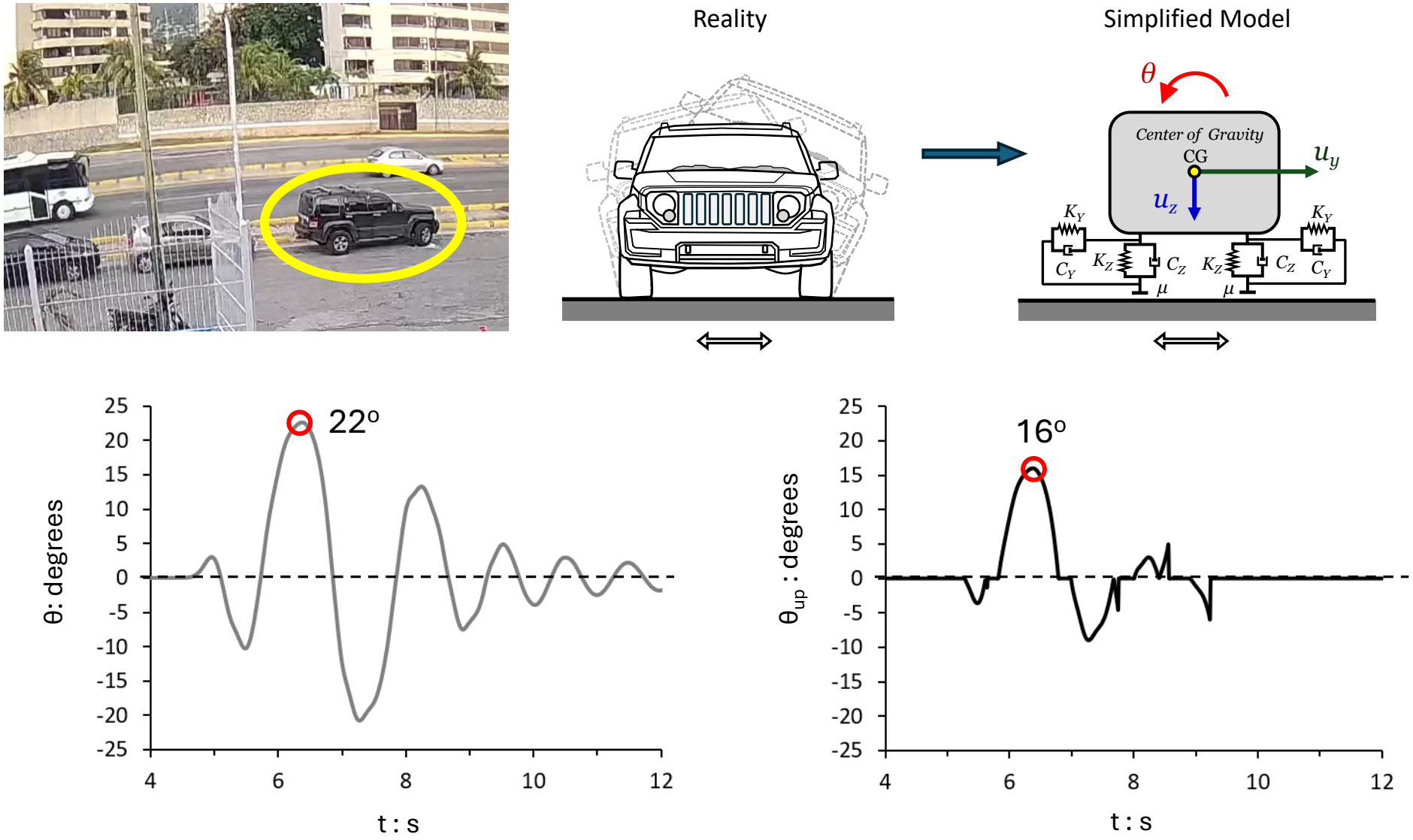


FIGURE 22 The heavy Jeep Cherokee/Liberty car and the computed angle of rotation time history caused by the **Fukiai-based** Gabor with $\mathbf{A_{Gabor}}$ **=0. 48 g**, $\mathbf{V_{Gabor}}$ **= 1.24 m/s.** [Vertical stiffness $K_z = 90\ kN/m$ per side]

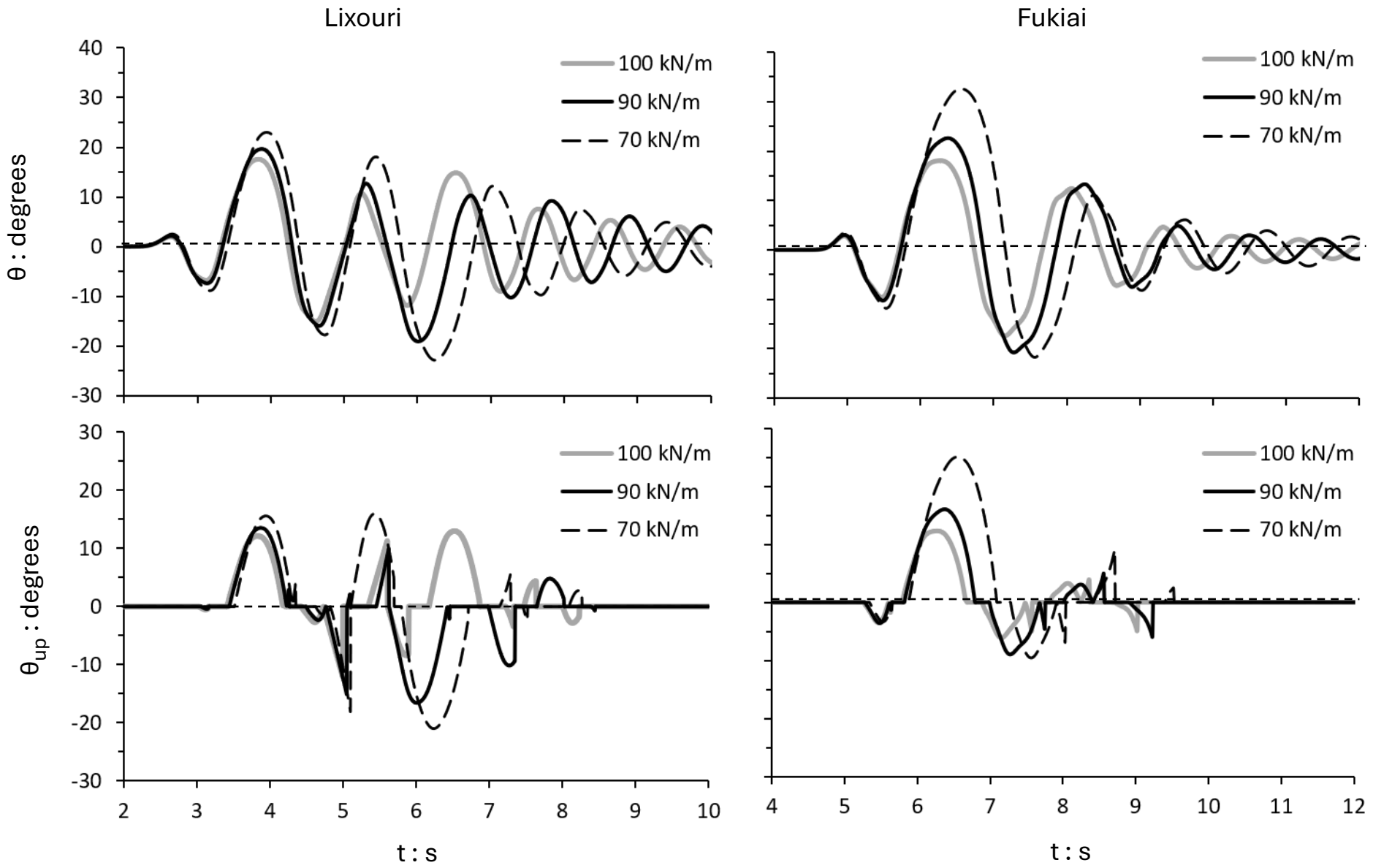


FIGURE 23 Influence of the vertical stiffness (K_z) of the heavy Jeep Cherokee/Liberty car on the total and uplifting angles caused by the **Lixouri-based Gabor** with $\mathbf{A_{Gabor}}$ **=0. 50 g**, $\mathbf{V_{Gabor}}$ **= 1.2 m/s** (left) and **Fukiai-based Gabor** with $\mathbf{A_{Gabor}}$ **=0. 48 g**, $\mathbf{V_{Gabor}}$ **= 1.24 m/s** (right), i.e. the motions that were compatible with the response angle of the light Daihatsu Terios car. Changing parametrically the K_z between 90 kN/m and 100 kN/m the two wavelets could lead to angle of rotation closer to the observed 14° – 20° .

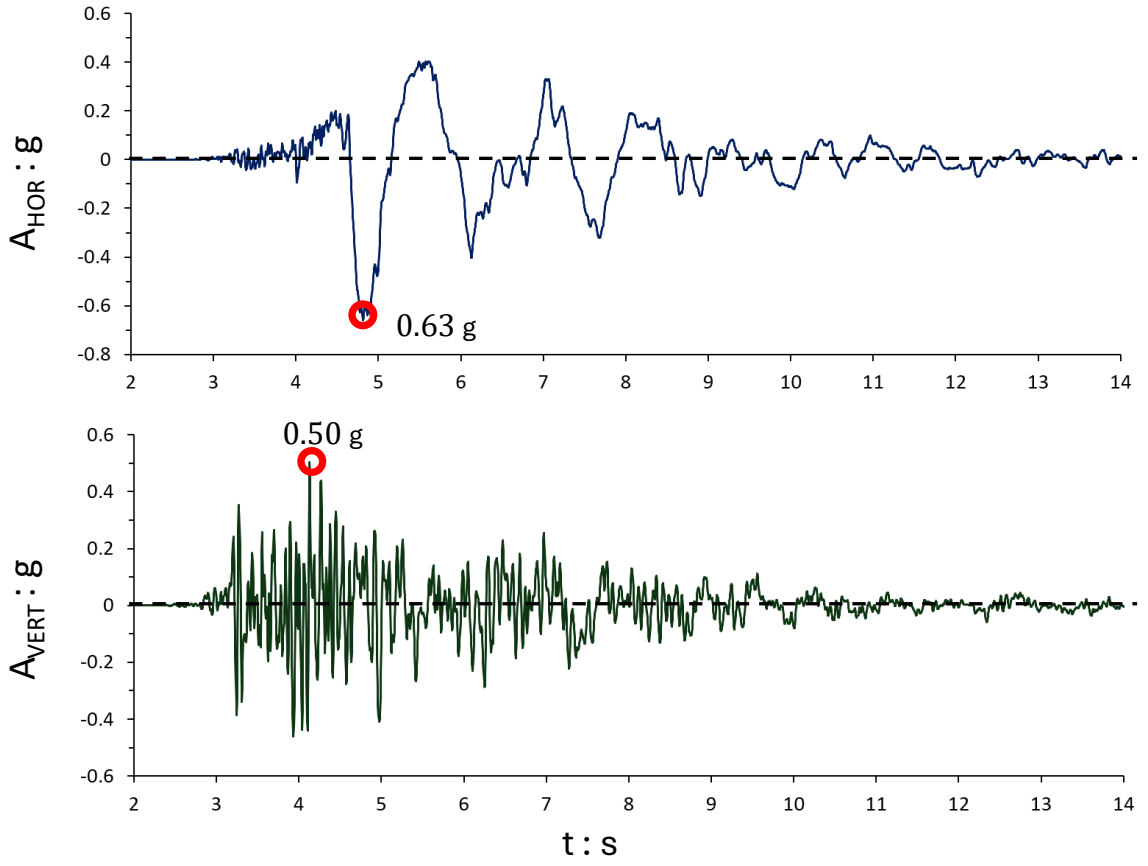


FIGURE 24 The recorded **horizontal** (EW) and **vertical** components of the **Lixouri** accelerogram.

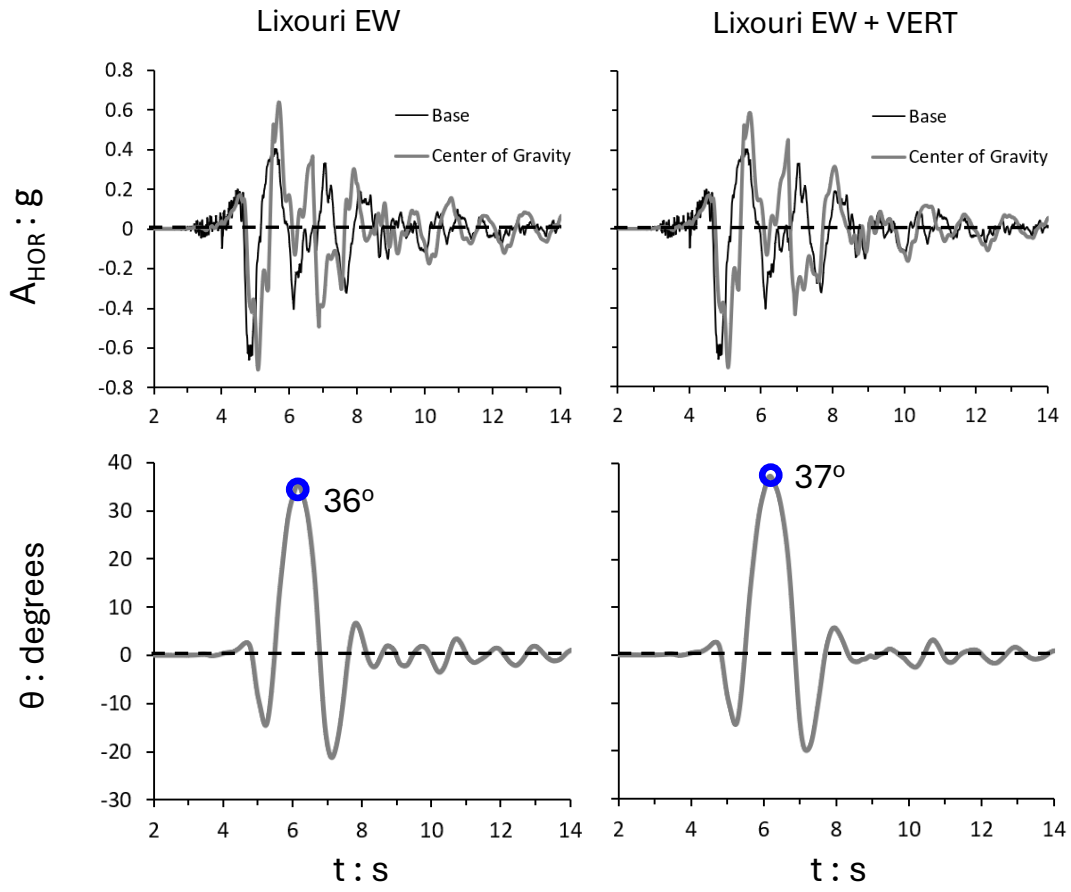
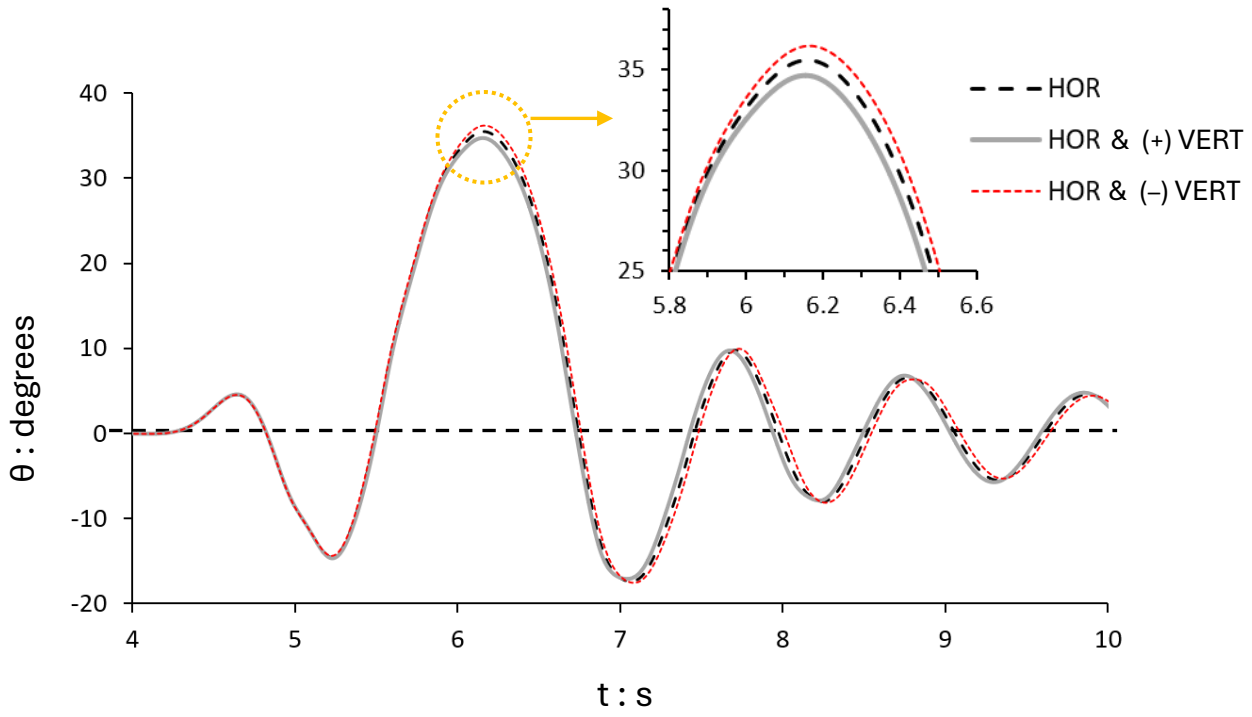


FIGURE 25 Comparison of seismic response of the light Daihatsu Terios due to either only the **horizontal** Lixouri EW (**as recorded**) component (Left), or simultaneously the **horizontal and vertical** (**as recorded**) components (Right)



Response parameter	HOR only	HOR & (+) VERT	HOR & (–) VERT
θ_{el}	12.7	13.4	11.5
θ_{upl}	27.5	26.8	28.7
θ	35.5	34.7	36.2

FIGURE 26 For the **fitted to Lixouri** components of asymmetric **Gabor** wavelets (horizontal and vertical) as excitation, the plots and the detailed Table summarize the response angles of rotation Daihatsu Terios car caused by: (i) the horizontal excitation only, and (ii) the simultaneous horizontal and vertical excitation; the latter with two opposite polarities (+ or −).